nature neuroscience

ARTICLES

https://doi.org/10.1038/s41593-019-0445-9

# Anterior cingulate cortex dysfunction underlies social deficits in *Shank3* mutant mice

Baolin Guo[1,8], Jing Chen[2,8], Qian Chen[3,8], Keke Ren[1], Dayun Feng[1,4], Honghui Mao[1], Han Yao[1], Jing Yang[1,5], Haiying Liu[1], Yingying Liu[1], Fan Jia[6], Chuchu Qi[1], Taylor Lynn-Jones[3], Hailan Hu[5], Zhanyan Fu[7], Guoping Feng[3*], Wenting Wang[1*] and Shengxi Wu[1*]

**Social deficit is a core clinical feature of autism spectrum disorder (ASD) but the underlying neural mechanisms remain largely unclear. We demonstrate that structural and functional impairments occur in glutamatergic synapses in the pyramidal neurons of the anterior cingulate cortex (ACC) in mice with a mutation in *Shank3*, a high-confidence candidate ASD gene. Conditional knockout of *Shank3* in the ACC was sufficient to generate excitatory synaptic dysfunction and social interaction deficits, whereas selective enhancement of ACC activity, restoration of SHANK3 expression in the ACC, or systemic administration of an α-amino-3-hydroxy-5-methyl-4-isoxazole propionic acid receptor-positive modulator improved social behavior in *Shank3* mutant mice. Our findings provide direct evidence for the notion that the ACC has a role in the regulation of social behavior in mice and indicate that ACC dysfunction may be involved in social impairments in ASD.**

Social behavior is critical for survival and reproduction in diversified species. It requires the processing of diverse information associated with sensory and reward information as well as cognition and emotion[1–3]. The integration of multiple sources of social information may be highly relevant to the function of the association cortex. The anterior cingulate cortex (ACC) has been recognized for its role in fundamental cognitive processes, including cost–benefit calculation, motivation and decision making[1,4]. Many studies performed in both humans and rodents have shown that the ACC is anatomically and functionally connected to a broad set of regions engaged in social information processing[1,5] and therefore likely to represent an information hub for the social network.

Social deficit is one of the core symptoms of patients with autism spectrum disorder (ASD). However, the neural substrates underlying these behavioral impairments are still not well understood, largely due to their inherent complexity[6,7]. Mutations in the Src-homology domain 3 (SH3) and multiple ankyrin repeat domains 3 (SHANK3) genes are monogenic causes of the neurodevelopmental disorder associated with ASD, and numerous mutations have been reported in both patients with ASD and those with Phelan–McDermid syndrome[8–10]. SHANK3 is a key excitatory postsynaptic scaffold protein that interacts with various postsynaptic density proteins. It plays an important role in targeting, anchoring and dynamically regulating postsynaptic neurotransmitter receptors and signaling molecules[8,11–13]. Previous studies from different research groups have consistently demonstrated that the deletion of *Shank3* in mice results in abnormal behaviors relevant to ASD, including repetitive behavior and social interaction deficits[13–23]. Furthermore, Mei et al. found that global re-expression of the *Shank3* gene in adult *Shank3*-deficient mice rescued repetitive behavior and social interaction deficits[21]. These results provided direct evidence supporting a causal link between *Shank3* deficiency and ASD-relevant behaviors.

Our previous study revealed that imbalanced dual-pathway activity in the striatum is responsible for repetitive grooming behavior in *Shank3* mutant mice[24]. In the current study, we investigated the neural substrates underlying social interaction deficits in *Shank3* mutant mice. The association cortices, such as the ACC and prefrontal cortex (PFC)[5,25–28], have been emphasized for their importance in social functions in previous studies of both patients and animal models. In particular, it has been reported that ascending projections from the mediodorsal thalamus to the medial PFC (mPFC) are relevant to social interaction[29] and social dominance[28]. Furthermore, PFC neurons that project to the nucleus accumbens (NAc) were found to encode social-spatial associations[27], while a PFC-habenular circuit was shown to be involved in social behavior and possibly associated with reward and emotion[30]. However, in our recent study, we found no detectable changes in the synaptic transmission of PFC pyramidal neurons in a *Shank3* mouse model carrying an ASD-linked InsG3680 mutation[23]. We thus decided to focus on characterizing the ACC and assessing whether ACC dysfunction is linked to social interaction deficits in the *Shank3* mutant mouse model.

In the current study, we found that *Shank3* deficiency leads to dendritic spine loss and impaired synaptic transmission and plasticity in ACC pyramidal neurons. The resulting hypoactivity of the pyramidal neurons in the ACC plays a causal role in social interaction deficits. Selective deletion of *Shank3* in the ACC sufficed to induce both synaptic dysfunction and social behavioral deficits that were comparable to those observed in global *Shank3* knockout (KO) mice. Selective activation of ACC pyramidal neurons with

[1]Department of Neurobiology, School of Basic Medicine, Fourth Military Medical University, Xi'an, China. [2]Department of Anatomy and K.K. Leung Brain Research Center, Fourth Military Medical University, Xi'an, China. [3]McGovern Institute for Brain Research, Department of Brain and Cognitive Sciences, Massachusetts Institute of Technology, Cambridge, MA, USA. [4]Department of Neurosurgery, Tangdu Hospital, Fourth Military Medical University, Xi'an, China. [5]Interdisciplinary Institute of Neuroscience and Technology, Qiushi Academy for Advanced Studies, Zhejiang University, Hangzhou, China. [6]Brain Research Center, State Key Laboratory of Magnetic Resonance and Atomic and Molecular Physics, Wuhan Institute of Physics and Mathematics, Chinese Academy of Sciences, Wuhan, China. [7]Stanley Center for Psychiatric Research, Broad Institute of MIT and Harvard, Cambridge, MA, USA. [8]These authors contributed equally: Baolin Guo, Jing Chen, Qian Chen. *e-mail: fengg@mit.edu; wwt0657@fmmu.edu.cn; shengxi@fmmu.edu.cn

optogenetics or chemogenetics, restoration of SHANK3 expression in ACC pyramidal neurons or systemic administration of an α-amino-3-hydroxy-5-methyl-4-isoxazole (AMPA) receptor-positive modulator to boost excitatory synaptic function significantly improved social behavior. Our findings provide direct evidence supporting a causal link between ACC dysfunction and social deficits in the *Shank3* mutant mouse model of ASD, and emphasize that the ACC is a potential therapeutic target for developing interventions for social deficits.

## Results

**SHANK3 deficiency alters the neuronal morphology of pyramidal neurons in the ACC.** To characterize *Shank3* expression in the ACC, we performed fluorescent in situ hybridization and immunofluorescent staining. *Shank3* messenger RNA and neuronal nuclear antigen (NeuN) or calcium/calmodulin-dependent protein kinase II (CaMKII) protein (Fig. 1a–c) displayed a strong colocalization pattern in the ACC. Additionally, the *Shank3* mRNA was also co-expressed with the GAD67 protein in a few neurons but was not co-expressed with either glial fibrillary acidic protein (GFAP) or Iba1, indicating that *Shank3* is predominantly expressed in pyramidal neurons in the ACC (Supplementary Fig. 1). Considering that SHANK3 plays critical roles in spine development and excitatory synaptic function[11,12,31], we sought to determine whether the *Shank3* deletion would induce structural and functional changes in the pyramidal neurons of the ACC, similar to what was observed in striatal medium spiny neurons in our previous studies[21,24]. First, we examined the dendritic processes and spines of ACC pyramidal neurons using either retroorbital injections of adeno-associated virus (AAV) 9-hSyn-EGFP-P2A-EGFPf (enhanced green flurescent protein farnesylated) or local injections of Semliki Forest virus (SFV) to sparsely label neurons with green fluorescent protein (GFP) in wild-type (WT) and *Shank3* KO mice[24,32,33]. We found that dendritic complexity and the densities of total spines and mushroom-shaped spines were significantly lower in the pyramidal cells of *Shank3* KO mice than in those of WT mice (Fig. 1d–j and Supplementary Fig. 2). Second, electron microscopy results indicated that the mean length and thickness of postsynaptic densities were significantly lower in *Shank3* KO mice than in WT mice (Fig. 1k–m). Together, these results indicate that the deletion of *Shank3* leads to structural defects in the dendrites and spines of ACC pyramidal neurons.

**SHANK3 deficiency alters the synaptic function of pyramidal neurons in the ACC.** To examine the functional consequences of SHANK3 deficiency on synaptic transmission in ACC, we performed whole-cell patch-clamp recording of pyramidal neurons. We found that the frequency and peak amplitude of α-amino-3-hydroxy-5-methylisoxazole-4-propionic acid receptor (AMPAR)-mediated miniature excitatory postsynaptic currents (mEPSCs) were significantly lower in *Shank3* KO mice than those in WT mice (Fig. 2a,b). Similarly, the evoked AMPAR-mediated EPSC amplitude and the AMPAR/NMDAR (*N*-methyl-D-aspartate receptor) ratio were lower in ACC pyramidal neurons in *Shank3* KO mice than those in WT mice (Fig. 2c–f). In contrast, the amplitudes of evoked NMDAR-mediated EPSCs were similar between WT and KO mice (Supplementary Fig. 3a,b). To examine whether a dysfunction in presynaptic release contributes to the observed synaptic defects, we performed paired-pulse ratio (PPR) analysis to detect any changes in the probability of presynaptic release. As shown in Supplementary Fig. 3c,d, we detected no differences in the PPR between genotypes when an inter-stimulus interval of 50 ms was applied. Furthermore, western blot analysis revealed that the *Shank3* KO mice expressed lower levels of the AMPAR subunit GluR1 than WT mice (Supplementary Fig. 4). AMPARs have been suggested to be crucial for the long-term potentiation (LTP) induced by pairing training paradigm in ACC pyramidal neurons[34]. We thus measured LTP in ACC pyramidal neurons and found that the paired training paradigm failed to induce LTP in KO mice (Fig. 2g,h).

Because the mPFC has a well-established role in social behaviors, we examined *Shank3* expression and synaptic transmission in mPFC pyramidal neurons in parallel. We found that the proportion of neurons expressing *Shank3* mRNA was comparable between the PFC and the ACC (Supplementary Fig. 5). Whole-cell patch-clamp recording of mEPSCs and the ratio of evoked AMPAR/NMDAR revealed no detectable differences in mPFC pyramidal neurons between WT and *Shank3* KO mice (Supplementary Fig. 6). These results indicate that *Shank3* deletion weakens the excitatory synaptic inputs to ACC but not mPFC pyramidal neurons.

**SHANK3 deficiency leads to hypoactivity in pyramidal neurons in the ACC.** We next directly tested whether defects in neuronal morphology and synaptic function in ACC pyramidal neurons would result in hypoactivity in ACC pyramidal neurons. First, we compared the capability of ACC pyramidal neurons to generate action potentials induced by excitatory postsynaptic potentials (EPSPs) between KO and WT mice. As expected, the ACC pyramidal neurons in the *Shank3* KO mice required a significantly higher presynaptic stimulation intensity to generate a spike from EPSPs (Fig. 3a–c). In addition to a reduced excitatory synaptic input level, alterations in intrinsic membrane properties may also contribute to the hypoactivity of ACC pyramidal neurons. We thus examined the intrinsic membrane properties of ACC pyramidal neurons. No significant differences in any parameters measured for the intrinsic membrane properties were found between WT and *Shank3* KO mice (Supplementary Fig. 7). We next performed a battery of behavioral tests, including a social interaction/preference test, novel object task, marble burying and open field test. As expected, we were able to recapitulate the phenotypes reported in our previous studies[15,21] (Supplementary Fig 8). We observed that *Shank3* KO mice showed robust defects in social interactions and social preference (Supplementary Fig. 8a–f). We then asked whether ACC pyramidal neurons would display hypoactivity in vivo during a social interaction task. We recorded real-time calcium dynamics in ACC pyramidal neurons in freely moving mice during the social interaction task via a fiber photometry system implanted in WT or KO mice expressing GCaMP3 (Fig. 3d,e and Supplementary Fig. 9). In line with previous slice electrophysiology results, we observed that ACC neuronal activity was significantly reduced in the *Shank3* KO mice when they approached unfamiliar mice (Fig. 3f–h and Supplementary Video 1).

**Selective deletion of *Shank3* in the ACC leads to social interaction deficits.** To provide a causal link between the observed hypoactivity of ACC pyramidal cells and social dysfunction, we selectively knocked out *Shank3* in the ACC by administering an AAV2/9 vector harboring *Staphylococcus aureus* Cas9 (SaCas9)[35] and a single-guide RNA (sgRNA) to adult WT mice to make a conditional knockout (CKO) of *Shank3* in the ACC (Fig. 4a). This CRISPR/Cas9-mediated genome-editing technique eliminated the major isoforms of SHANK3, including its putative α, β and γ isoforms, specifically in the ACC but not in the adjacent motor cortex (Fig. 4b–d and Supplementary Fig. 10). Consistent with the results obtained in global *Shank3* KO mice, *Shank3* CKO in ACC pyramidal neurons resulted in reduction in mEPSCs frequency and peak amplitude, a decrease in input-output responses of evoked AMPAR-mediated EPSCs and a lower AMPAR/NMDAR ratio compared to the WT controls. A comparable PPR was observed between the genotypes, suggesting that the presynaptic release probability was unaltered in CKO mice (Fig. 4e–l). Western blot analysis showed that the expression of the AMPAR GluR1 and GluR2 subunit was significantly lower in the ACC of CKO mice than that in the ACC of WT mice. In contrast, the expression of NMDAR subunit NR2B

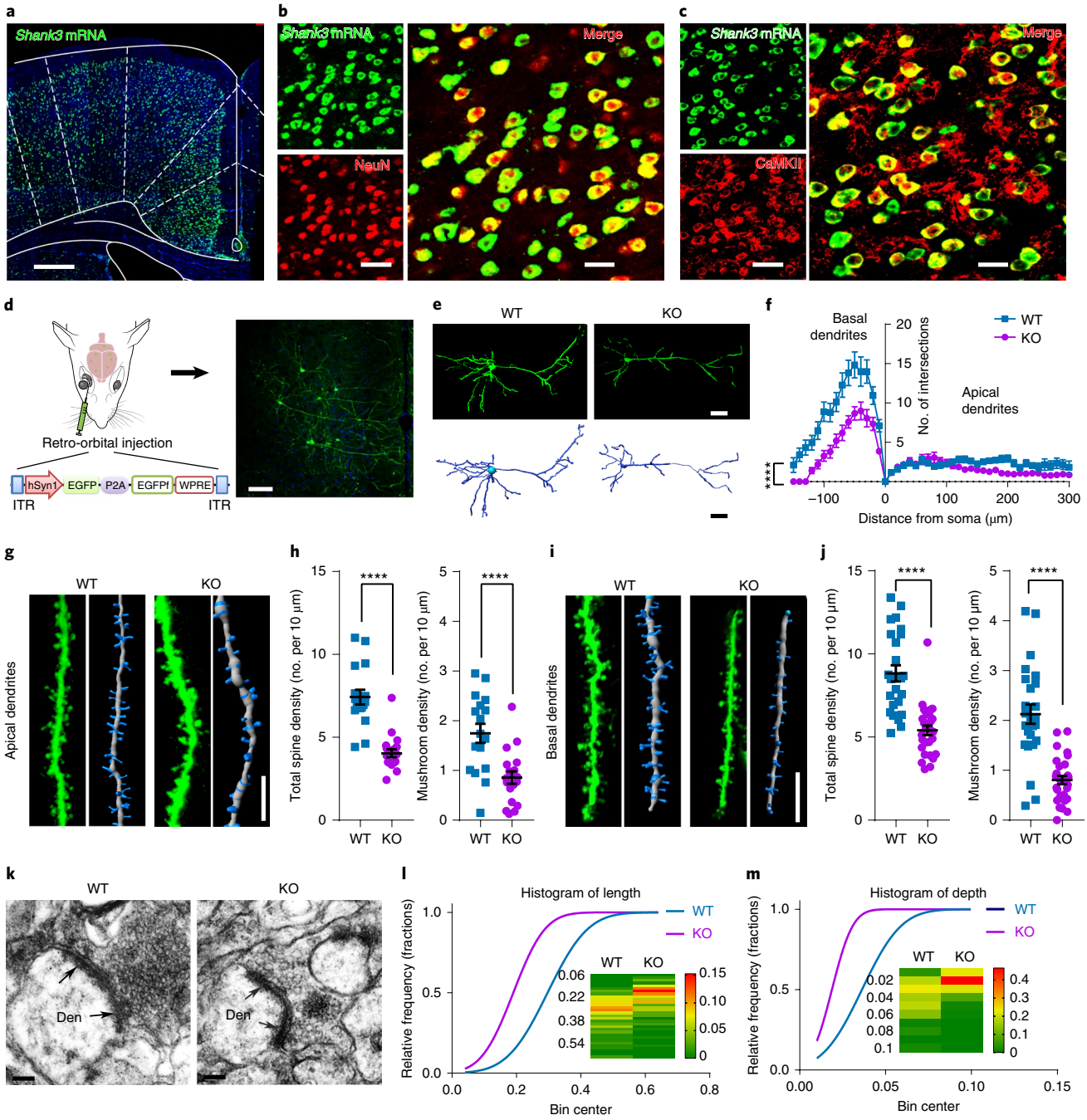


**Fig. 1 | Morphological changes in the ACC of *Shank3* KO mice. a**, A low-magnification image showing the distribution of the *Shank3* mRNA in the ACC. Scale bar, 300 μm. **b**, Fluorescence in situ hybridization and immunohistochemistry double staining shows that the *Shank3* mRNA colocalizes with NeuN. Scale bars, 50 μm (left) and 25 μm (right). **c**, Fluorescence in situ hybridization and immunohistochemistry double staining shows that the *Shank3* mRNA colocalizes with CaMKII. Scale bars, 50 μm (left) and 25 μm (right). **d**, Schematic of the retroorbital injection method used to sparsely label neurons (left). A representative image showing sparsely labelled neurons in the ACC (right). Scale bar, 100 μm. **e**, Representative pyramidal neurons in the ACC in KO and WT mice. Scale bars, 50 μm. **f**, Sholl analysis of dendritic branching complexity in the basal and apical dendrites of WT and KO mice (WT: $n=18$ neurons from four mice; KO: $n=15$ neurons from three mice. Friedman's *M*-test). **g**, Representative confocal stacks and three-dimensional reconstruction images of the apical dendrites of ACC pyramidal neurons obtained from both WT and KO mice. Scale bar, 10 μm. **h**, Summary of spine density on the apical dendrites of ACC pyramidal neurons obtained from WT and KO mice (WT: $n=17$ dendrites from four mice; KO: $n=19$ dendrites from three mice. Total spine density: Mann–Whitney *U*-test; mushroom density: two-tailed unpaired *t*-test). **i**, Representative confocal stacks and three-dimensional reconstruction images of ACC pyramidal neuronal basal dendrites in KO and WT mice. Scale bar, 10 μm. **j**, The spine density on basal dendrites was lower in KO mice than in WT mice (WT: $n=25$ dendrites from four mice; KO: $n=29$ dendrites from three mice. Total spine density: Mann–Whitney *U*-test; mushroom density: two-tailed unpaired separate variance estimation *t*-test). **k**, Representative electron micrographs showing the synaptic structure and postsynaptic densities on neurons (arrowheads). Scale bars, 100 nm. **l**, The lengths of postsynaptic densities were shorter in KO mice than in WT mice (WT: $n=98$ synapses from six mice; KO: $n=144$ dendrites from six mice). **m**, The depths of postsynaptic densities were shallower in KO mice than in WT mice (WT: $n=98$ synapses from six mice; KO: $n=144$ dendrites from six mice). **a**–**c** were independently repeated five times and **d** was independently repeated four times for WT and three times for KO with similar results obtained. Data are presented as the mean ± s.e.m. See Supplementary Table 2 for detailed statistical information. ****$P<0.0001$.

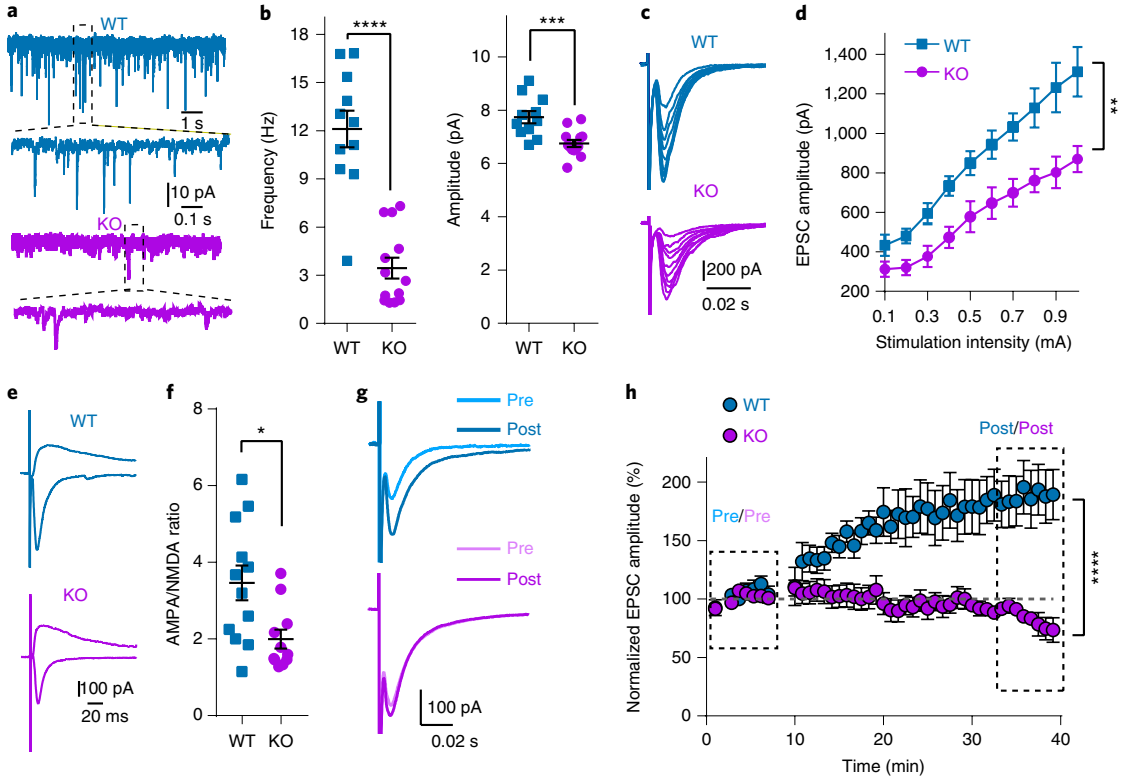


**Fig. 2 | Excitatory synaptic dysfunction in the ACC pyramidal neurons of *Shank3* KO mice. a**, Representative mEPSCs traces in ACC pyramidal neurons in WT and KO mice. **b**, Summary data for mEPSCs frequency and peak amplitude in ACC pyramidal neurons obtained from WT and KO mice (WT: $n=11$ neurons from three mice; KO: $n=13$ neurons from three mice. Frequency: Mann–Whitney *U*-test; amplitude: two-tailed unpaired *t*-test). **c**, Representative trace of AMPAR-mediated evoked EPSCs in ACC pyramidal neurons obtained from WT and KO mice. **d**, Summary data for the peak amplitudes of evoked AMPAR-EPSCs in response to different levels of stimulation intensity (WT: $n=5$ neurons from two mice; KO: $n=5$ neurons from two mice. Repeated measurement ANOVA). **e**, Representative trace of AMPAR/NMDAR EPSCs ratio in WT and KO mice. **f**, Summary data for the AMPAR/NMDAR EPSC ratio in ACC pyramidal neurons in WT and KO mice (WT: $n=12$ neurons from three mice; KO: $n=11$ neurons from three mice. Mann–Whitney *U*-test). **g**, Averaged traces from LTP recordings. Light traces represent the baseline EPSC (averaged from the dashed box) and dark traces represent the post-induction EPSC (averaged from the dashed box after LTP induction). **h**, The ACC pyramidal neurons of KO mice showed impaired LTP when compared to WT mice (WT: $n=10$ neurons from ten mice; KO: $n=10$ neurons from ten mice. Friedman's *M*-test). Data are presented as the mean ± s.e.m. See Supplementary Table 2 for detailed statistical information. $^*P<0.05$, $^{**}P<0.01$, $^{***}P<0.001$, $^{****}P<0.0001$.

was higher in the ACC of CKO of mice (Supplementary Fig. 11). When the three-chamber test and social interaction test were performed to probe animals for their abilities to discriminate social novelty (three-chamber test) and voluntary initiation of social interaction (social interaction test in the home cage), we found that the CKO mice displayed dysfunctional social interaction behavior, as measured by both in time spent in the compartment containing the stranger mouse and direct interaction time with the novel mouse in the home cage (Fig. 4m–p), while all other measured behavioral phenotypes—including grooming, marble burying, behavior in the novel object task and anxiety levels—were comparable to those of the WT controls (Supplementary Fig. 12). These results indicate that *Shank3* deficiency in the ACC alone is sufficient to induce social interaction deficits.

**Optogenetic activation of ACC improved social behaviors in *Shank3* mutant mice.** We next selectively enhanced the activity of ACC pyramidal neurons by using AAV2/8-CaMKIIa-hChR2-EYFP to deliver channelrhodopsin-2 (ChR2) to pyramidal neurons in the ACC (Fig. 5a,b). On the basis of previous studies that used in vivo recordings in ACC pyramidal neurons[36], the firing rates of ACC pyramidal neurons during the free moving state were less than 10 Hz. In both in vitro whole-cell recording and in vivo optrode recording, we found that ACC pyramidal neurons expressing ChR2 fired action potentials faithfully in response to 10 Hz of photostimulation with a 473-nm laser (Fig. 5c,d). As expected, 10 Hz of photostimulation induced obvious c-Fos expression in the ipsilateral site to the virus injection but not in the contralateral site (Fig. 5e). When the ACC was optogenetically activated, *Shank3* KO mice spent significantly more time in the compartment of the stranger mouse (Fig. 5f–h) or initiated more social interaction with the novel partner in the home cage than the EYFP (enhanced yellow fluorescent protein) controls (Fig. 5i–k, Supplementary Fig. 13 and Supplemental Video 2). Such an increased sociability was also observed in WT mice during photostimulation of ACC pyramidal cells (Supplementary Fig. 14). Additionally, optical activation of the ACC induced anxiolytic effects for both WT and KO mice (Fig. 5l,m and Supplementary Fig. 14). We also tested the social behavior outcomes that were triggered by lower and higher light frequencies (that is, 5 and 20 Hz light stimulation) and found that 5 Hz was not enough to ameliorate the social deficits observed in *Shank3* KO mice, whereas 20 Hz induced an increase in the social activities and social preferences of *Shank3* KO mice (Supplementary Fig. 15). Next, we tested whether optogenetic inhibition of ACC pyramidal neurons in WT mice would be sufficient to mimic the social deficits observed in *Shank3* KO mice. We found that photoinhibition of ACC pyramidal neuronal activity in WT mice with NpHR induced impairments in social interaction and social preference (Supplementary Fig. 16). However, ACC photoinhibition did not affect anxiety-like behavior (Supplementary Fig. 16). Taken together,

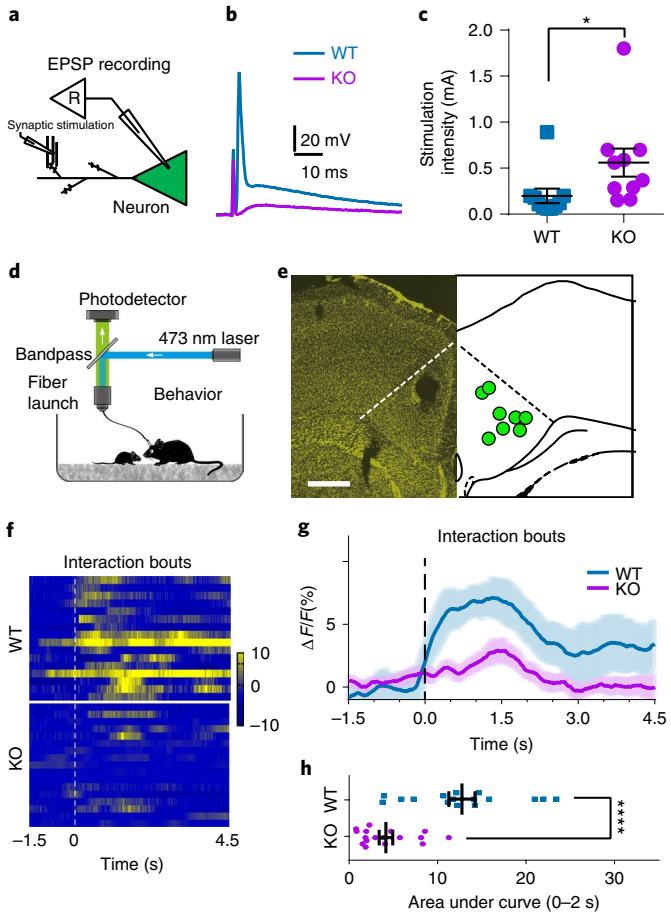


**Fig. 3 | ACC pyramidal neurons show weaker responses to initial social contact in *Shank3* KO mice. a**, Schematic of an EPSP recording. **b**, Representative EPSP traces from WT and KO mice. **c**, ACC pyramidal neurons of KO mice required significantly higher presynaptic stimulation intensity to generate action potential than was required for WT ACC pyramidal neurons (WT: $n=10$ neurons from three mice; KO: $n=10$ neurons from three mice). **d**, Schematic of the procedure used to record calcium signaling activity in GCaMP-expressing neurons using fiber photometry. **e**, Optic fiber placement. Scale bar, 500 µm. **f**, Heat map illustrating the calcium response ($\Delta F/F$, %) of ACC pyramidal neurons during social interaction. **g**, Peri-event plots of averaged calcium signals. Solid line and the shaded regions are the mean ± s.e.m. **h**, The activity signal on social interaction with a juvenile mouse was significantly weaker in ACC pyramidal neurons in KO mice than those in WT mice. **g**,**h**, WT: $n=16$ trials from four mice; KO: $n=17$ trials from four mice. Data are presented as the mean ± s.e.m. Statistical analyses in **c** and **g** were performed using the Mann–Whitney *U*-test. See Supplementary Table 2 for detailed statistical information. $^{**}P<0.01$, $^{****}P<0.0001$.

these results demonstrate that the ACC bidirectionally regulates social behaviors but unidirectionally regulates anxiety behaviors.

In addition, we examined whether the activation of ACC pyramidal neurons could reduce repetitive self-grooming behavior, which is another core phenotype of the *Shank3* KO mouse model. Because repetitive self-grooming must be scored over an extended period of time (2 h), we applied designer receptors that would be exclusively activated by designer drugs (DREADDs) to enhance ACC pyramidal cell activity. We injected a mixture of AAV2/8-CaMKIIa-Cre-EGFP and AAV2/8-EF1a-DIO-hM3D(Gq)-mCherry into the ACC and verified that hM3Dq was expressed in ACC pyramidal neurons (Supplementary Fig. 17). In line with the improvement in social interactions by optogenetic activation, administration of 0.7 mg kg$^{-1}$ clozapine N-oxide (CNO) corrected the social interaction deficits (Supplementary Fig. 18a–d). However, we did not observe any alterations in grooming bouts or duration in *Shank3* KO mice (Supplementary Fig. 18e–h). These results demonstrate that selective activation of pyramidal neurons in the ACC improves social function but not improve repetitive grooming behavior in the *Shank3* KO mouse model of ASD.

**Selective restoration of SHANK3 in the ACC ameliorates social deficits in *Shank3* mutant mice.** Our previous study showed that global re-expression of the *Shank3* gene in adult mice led to improvements in synaptic protein composition, spine density, synaptic function and certain behavioral abnormalities, including social interaction deficits and repetitive grooming behavior by generating a conditional knock-in (CKI) *Shank3* mouse model in which exon 13–16 encoding the PDZ domain, were inverted with a Flex system[21]. Then we tested whether selectively restoring SHANK3 expression in the ACC of adult *Shank3* CKI mice would rescue social interaction deficits. We injected AAV2/8-CaMKII-Cre-EGFP into the ACC of CKI mice to re-express most SHANK3 isoforms in the ACC but not the adjacent motor cortex (Fig. 6a–c and Supplementary Fig. 19). Basal synaptic transmission measurements indicated that in the AAV-infected ACC pyramidal cells, there was a partial rescue of mEPSC frequency but a full restoration of mEPSC peak amplitude and the input–output responses of AMPAR-mediated EPSCs as well as the AMPAR/NMDAR ratio (Fig. 6d,e,h–k). Again, there was no difference in the PPR between WT and CKI mice infected with AAV2/8-CaMKII-Cre-EGFP (Fig. 6f,g). Consistent with electrophysiology results, we found that total spine density and mushroom spine density were significantly increased after AAV-Cre infection (Supplementary Fig. 20). The reduced protein levels of GluR1, GluR2 and NR2B were also rescued by Cre-mediated *Shank3* gene restoration (Supplementary Fig. 21). Again, our behavioral tests demonstrated that re-expression of *Shank3* in the ACC alone was sufficient to rescue the observed social interaction deficit (Fig. 6i–p) but not repetitive grooming behavior and anxiety-like behavior (Supplementary Fig. 22) of *Shank3* CKI mice. These results further support the notion that the ACC plays an important role in social behavior.

**Pharmacological enhancement of AMPARs improves social deficits in *Shank3* mutant mice.** Given that the profound defect in AMPAR function is the major cause of hypoactivity of the ACC in *Shank3* KO mice, we sought to test whether correcting the reduction in AMPAR activity could potentially improve the social deficits observed in *Shank3* KO mice. CX546 is an AMPAKINE compound containing a benzamide core and a six-carbon ring and acts as an AMPAR-positive allosteric modulator (PAM, Fig. 7a). We found that the application of CX546 increased both amplitude and duration of AMPAR currents (Fig. 7b–d). We next subcutaneously injected CX546 at three different dosages in *Shank3* KO mice over 7 d, followed by behavioral tests and excitatory synaptic activity measurements in vitro at the eighth day post-administration (Fig. 7a). The dosage selection and treatment duration were designed based on previous reports to achieve a balance between enhancement of AMPAR activity and minimal potential side effects[37,38]. We found that administration of CX546 at concentrations of 10 and 20 mg kg$^{-1}$ but not 5 mg kg$^{-1}$ improved social preference and social interaction in *Shank3* KO mice (Fig. 7e–h and Supplementary Fig. 23). To further confirm that ACC was involved in the effect of systemic administration of CX546, we microinjected CX546 (400 µM) into the ACC and tested social novelty responses in the KO mice. We found that CX546 infusion in ACC also ameliorated social deficits in both three-chamber test and social interaction test in the home cage in *Shank3* KO mice (Supplementary Fig. 24). ACC pyramidal neurons in acute brain slices from *Shank3* KO mice treated with 10 mg kg$^{-1}$

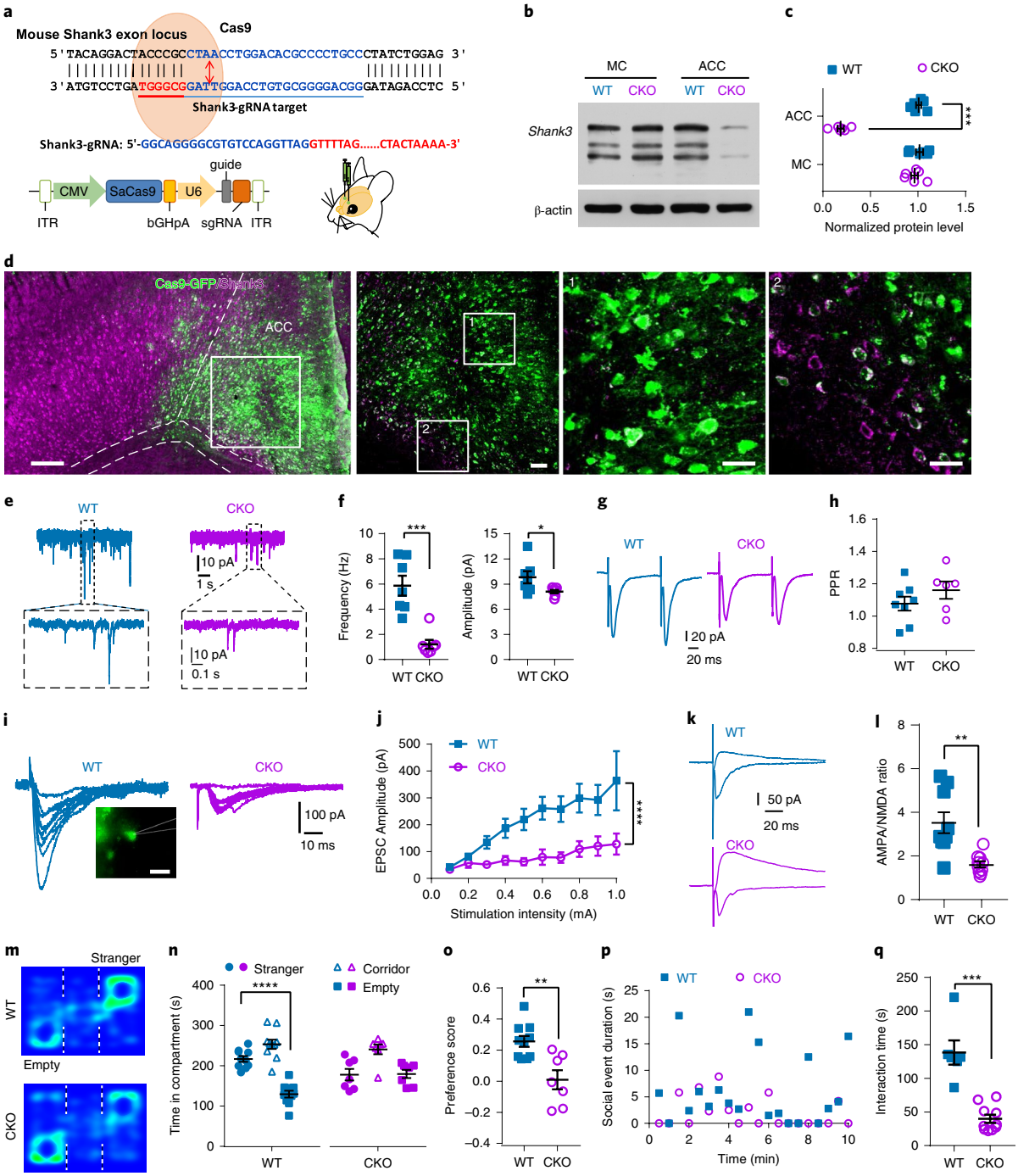


**Fig. 4 | Conditional *Shank3* deletion in the ACC recapitulates synaptic impairments and social dysfunction. a**, Schematic representations of *Shank3* target sites and the Cas9 AAV vector. **b**,**c**, Western blot analysis showing specific *Shank3* KO in the ACC, with minimal effects on the neighboring motor cortex (MC) (WT: $n=6$ mice; CKO: $n=6$ mice. ACC and MC: two-tailed unpaired *t*-test). See Supplementary Fig. 25a for gel source data. **d**, Immunohistochemistry staining confirms the selective KO of *Shank3* in GFP-expressing neurons of the ACC but not in GFP-negative neurons. Scale bars, 50 μm (two images on the left) and 25 μm (two images on the right). **e**,**f**, ACC pyramidal neurons in CKO mice exhibited mEPSCs with lower frequencies and peak amplitudes than those observed in WT mice (WT: $n=7$ neurons from two mice; CKO: $n=7$ neurons from two mice. Frequency: Mann–Whitney *U*-test; amplitude: two-tailed unpaired *t*-test). **g**,**h**, The PPR of evoked EPSCs in the ACC of CKO mice was similar to that obtained in the WT group (WT: $n=8$ neurons from two mice; CKO: $n=6$ neurons from two mice. Two-tailed unpaired *t*-test). **i**,**j**, The EPSCs evoked from the ACC had smaller amplitudes in CKO mice than in WT mice. The inset image shows an infected neuron with a micropipette (WT: $n=8$ neurons from two mice; CKO: $n=8$ neurons from two mice. Friedman's *M*-test. Scale bar, 25 μm). **k**,**l**, The AMPAR/NMDAR ratio was lower in CKO ACC pyramidal neurons than in WT ACC pyramidal neurons (WT: $n=9$ neurons from three mice; CKO: $n=10$. neurons from three mice. Two-tailed unpaired separate variance estimation *t*-test). **m**, Representative heatmaps of the three-chamber test performed in WT and CKO mice. **n**, CKO mice did not show social novelty in three-chamber test (WT: $n=10$ mice; CKO: $n=7$ mice. WT: one-factor ANOVA with Tukey's multiple comparisons test. CKO: Kruskal–Wallis *H*-test with Nemenyi multiple comparisons test). **o**, CKO mice showed reduced social preference (WT: $n=10$ mice; CKO: $n=7$ mice. Two-tailed unpaired *t*-test). **p**, Representative time course of the interaction time. **q**. CKO mice spent less time interacting with the unfamiliar mice (WT: $n=6$ mice; CKO: $n=10$ mice. Mann–Whitney *U*-test). Data are presented as the mean ± s.e.m. See Supplementary Table 2 for detailed statistical information. $^*P<0.05$, $^{**}P<0.01$, $^{***}P<0.001$, $^{****}P<0.0001$.

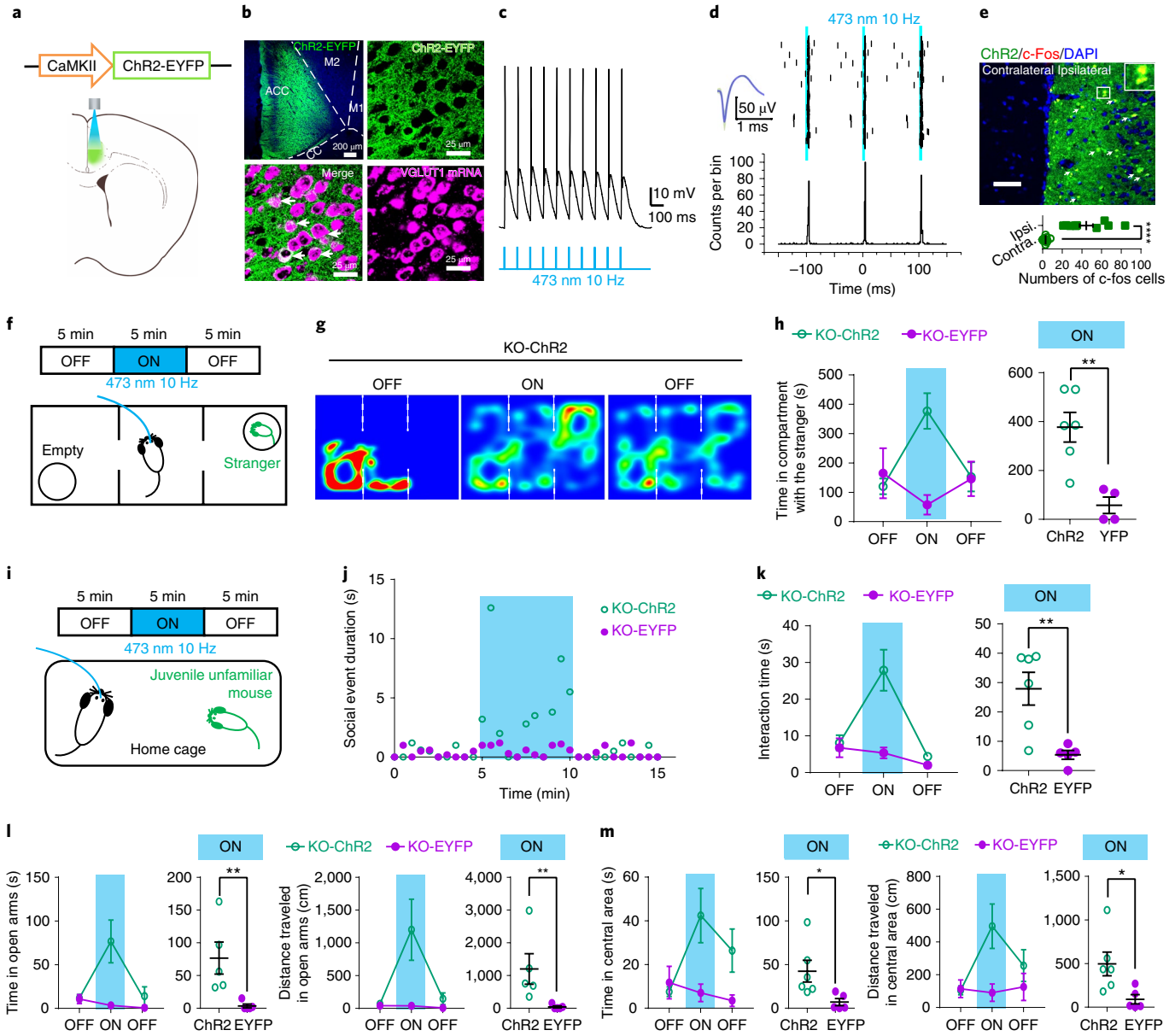


**Fig. 5 | Optogenetic activation of ACC pyramidal neurons rescues social interaction and anxiety behaviors in KO mice. a**, Diagram of ACC photoactivation (left) and photomicrograph of ChR2 expression (right). **b**, ChR2-expressing neurons in the ACC with post hoc fluorescence in situ hybridization for the vesicular glutamate transporter 1 mRNA. The experiment was independently repeated five times with similar results obtained. Scale bars: top left, 200 μm, bottom left, 20 μm (left) and 25 μm (right), bottom right, 25 μm. **c**, Whole-cell recordings showing that ACC pyramidal neurons exhibited faithful activation in response to 10 Hz of optogenetic stimulation. The experiment was independently repeated in seven neurons from two mice with similar results obtained. **d**, Raster plots (top) and peristimulus histogram (bottom) of data obtained from an in vivo optrode recording of a single neuron showed reliable responses to 10 Hz of blue light stimulation. The insert shows the average spike waveform from the same neuron. The experiment was independently repeated in 15 units from three mice with similar results obtained. **e**, ChR2-expressing neurons colocalized with c-Fos-expressing neurons in the ipsilateral site to ChR2 injection but not in the contralateral site (top panel: representative image; bottom panel: summary data; Ctrl: $n=10$ slices from three mice; Ipsi: $n=10$ slices from three mice. Two-tailed unpaired separate variance estimation $t$-test). Scale bar, 50 μm. **f**, Schematic of the three-chamber test and laser delivery strategy. **g**, Representative heat maps. **h**, Compared with the KO-EYFP mice, the KO-ChR2 mice spent significantly more time in the stranger compartments (KO-ChR2: $n=6$ mice; KO-EYFP: $n=4$ mice. Two-tailed unpaired $t$-test). **i**, Schematic of the home-cage social interaction task and laser delivery strategy. **j**, Representative time course of the interaction time observed in KO-ChR2 and KO-EYFP mice. **k**, Summary data showing that KO-ChR2 mice had significantly longer interaction times with unfamiliar mice during photoactivation than was observed in the KO-EYFP mice (KO-ChR2: $n=6$ mice; KO-EYFP: $n=5$ mice. Two-tailed unpaired separate variance estimation $t$-test). **l**, Summary data of the elevated plus maze test showing that KO-ChR2 mice spent more time (left panel) and traveled longer distances in the open arms (right panel) than were observed for the KO-EYFP mice (KO-ChR2: $n=5$ mice; KO-EYFP: $n=5$ mice. Time and distance: Mann–Whitney $U$-test). **m**, Summary data of the open field test showing that KO-ChR2 mice spent more time and traveled longer distances in the central zones than were observed for the KO-EYFP mice (KO-ChR2: $n=6$ mice; KO-EYFP: $n=5$ mice. Time and distance: two-tailed unpaired $t$-test). Data are presented as the mean ± s.e.m. See Supplementary Table 2 for detailed statistical information. $^{*}P<0.05$, $^{**}P<0.01$, $^{****}P<0.0001$.

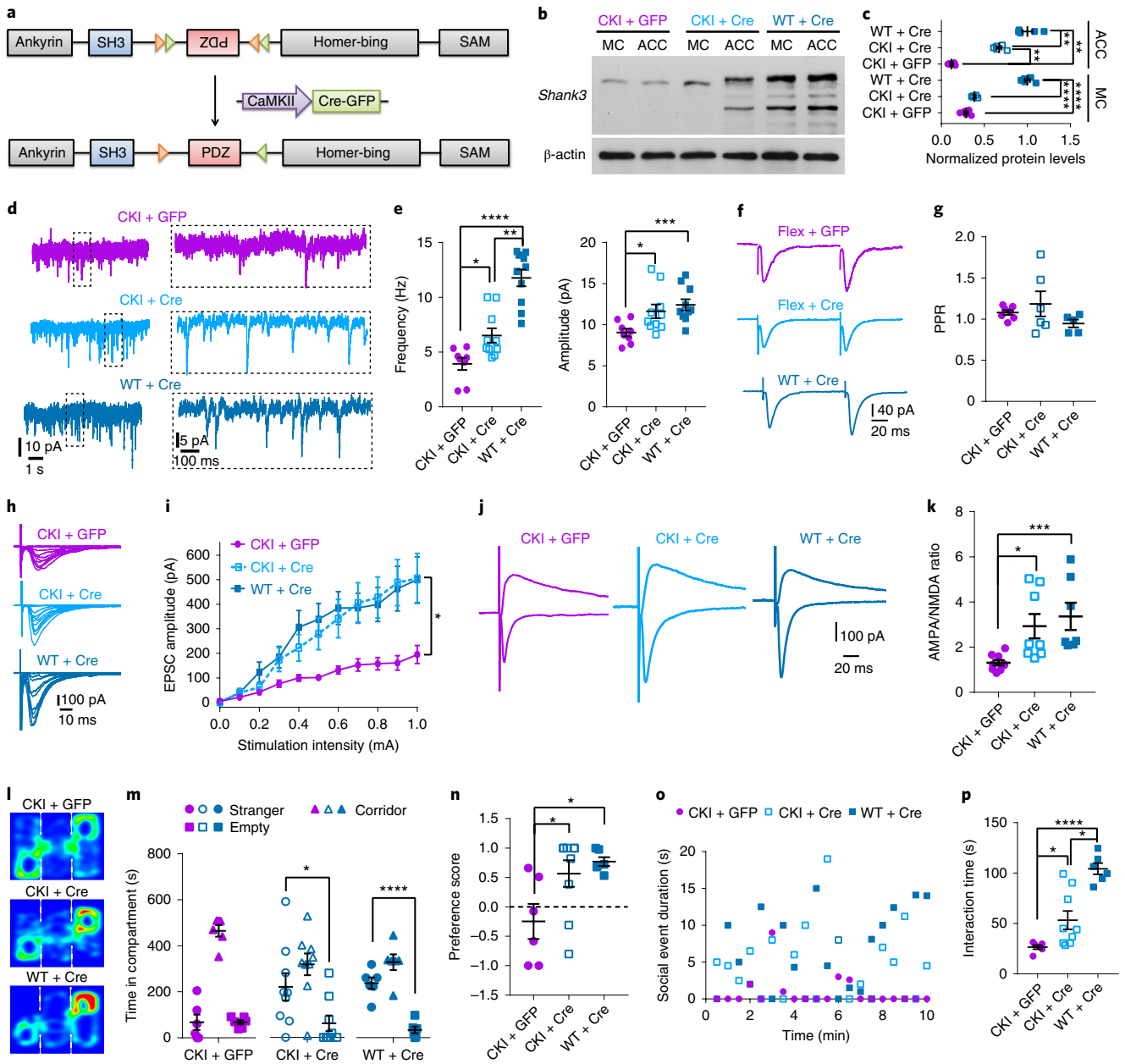


**Fig. 6 | Adult restoration of *Shank3* expression in the ACC partially rescues synaptic impairments and social dysfunction. a**, Working strategy to explore the adult re-expression of *Shank3* induced using a *Shank3* conditional knock-in mouse model (CKI). **b**,**c**, Western blot analysis confirmed that SHANK3 was specifically expressed in the ACC but not in the motor cortex (MC) (CKI + GFP: $n = 5$ mice; CKI + Cre: $n = 5$ mice; WT + Cre: $n = 5$ mice. ACC: Kruskal–Wallis *H*-test with Nemenyi multiple comparisons test; MC: one-factor ANOVA with Tukey's multiple comparisons test). See Supplementary Fig. 25a for gel source data. **d**, Representative traces of mEPSCs recorded in the ACC in the three experimental groups. **e**, Summary data showing the partial rescue of the mEPSCs frequency and peak amplitude in CKI + Cre mice but not the CKI + GFP mice (CKI + GFP: $n = 8$ neurons from three mice; CKI + Cre: $n = 10$ neurons from three mice; WT + Cre: $n = 10$ neurons from three mice. Frequency and amplitude: Kruskal–Wallis *H*-test with Nemenyi multiple comparisons test). **f**, Representative traces of the PPR in all groups. **g**, The PPR did not show differences among any of the groups (CKI + GFP: $n = 7$ neurons from four mice; CKI + Cre: $n = 6$ neurons from four mice; WT + Cre: $n = 5$ neurons from three mice. Kruskal–Wallis *H*-test). **h**, Example traces of evoked EPSCs in all three groups. **i**, Summary data of the inputs-outputs of evoked EPSC amplitudes on different levels of stimulation intensity in all three groups of mice (CKI + GFP: $n = 7$ neurons from four mice; CKI + Cre: $n = 6$ neurons from four mice; WT + Cre: $n = 6$ neurons from four mice. Friedman's *M*-test). **j**, Representative trace of an AMPAR/NMDAR-mediated EPSC. **k**, The AMPAR/NMDAR EPSC ratio was partially rescued in CKI + Cre mice but not the CKI + GFP mice (CKI + GFP: $n = 9$ neurons from three mice; CKI + Cre: $n = 8$ neurons from three mice; WT + Cre: $n = 7$ neurons from three mice. Kruskal–Wallis *H*-test with Nemenyi multiple comparisons test). **l**, Representative heatmaps of the three-chamber test in all groups. **m**,**n**, Summary data of the time spent in the compartment and the preference scores for all three groups of mice (CKI + GFP: $n = 6$ mice; CKI + Cre: $n = 9$ mice; WT + Cre: $n = 6$ mice. CKI + GFP and WT + Cre: one-factor ANOVA with Tukey's multiple comparisons test. CKI + Cre: Kruskal–Wallis *H*-test with Nemenyi multiple comparisons test. Preference score: Kruskal–Wallis *H*-test with Nemenyi multiple comparisons test). **o**, Example time course plotting of social events in all three groups of mice. **p**, Summary data showing averaged total interaction times with an unfamiliar mouse in all three groups of mice (CKI + GFP: $n = 6$ mice; CKI + Cre: $n = 9$ mice; WT + Cre: $n = 6$ mice. Kruskal–Wallis *H*-test with Nemenyi multiple comparisons test). Data are presented as the mean ± s.e.m. See Supplementary Table 2 for detailed statistical information. $^{*}P < 0.05$, $^{**}P < 0.01$, $^{***}P < 0.001$, $^{****}P < 0.0001$.

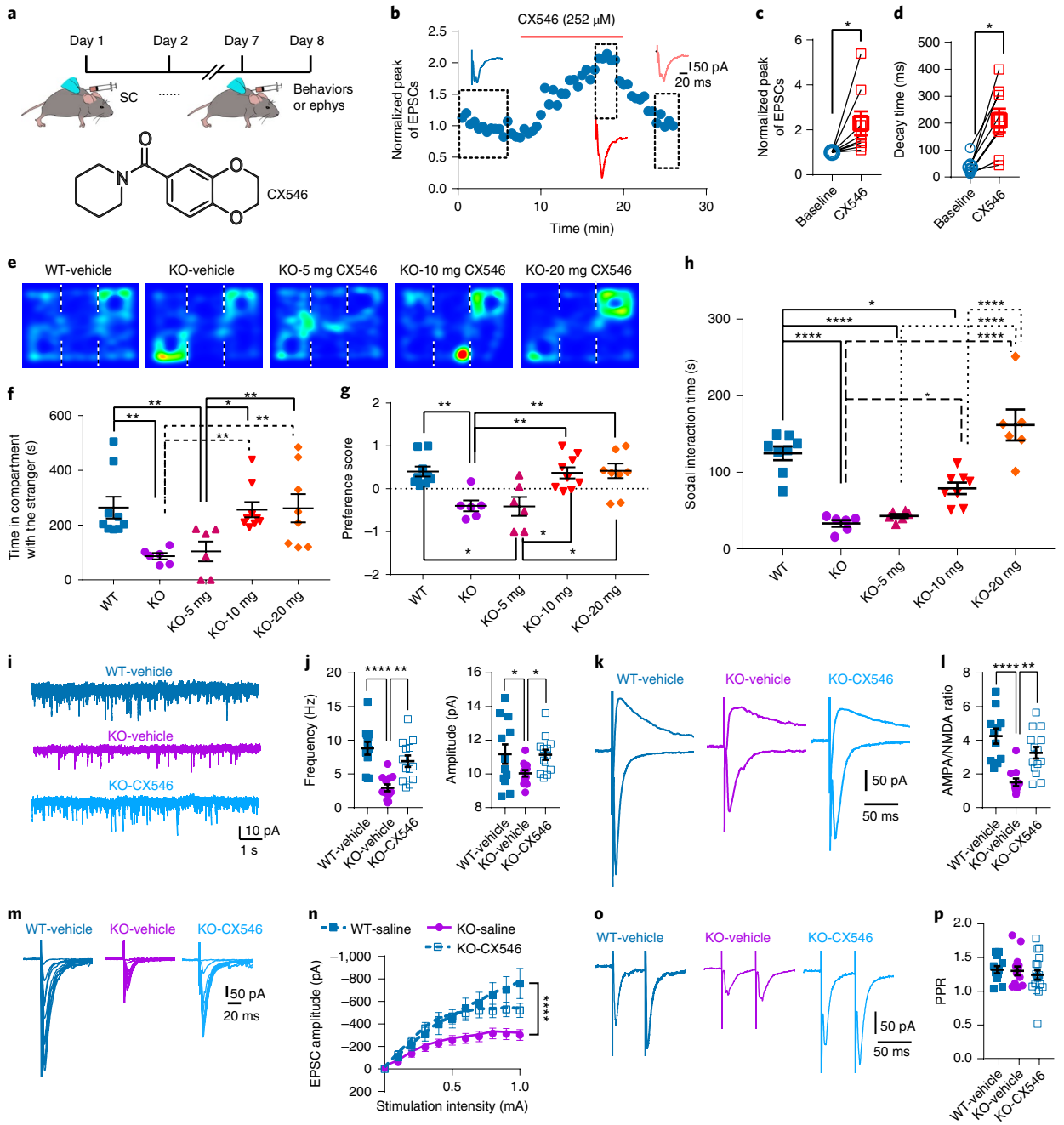


**Fig. 7 | Systemic administration of an AMPA receptor-positive modulator improves social behaviors in KO mice. a**, Experimental paradigm of CX546 administration via subcutaneous (SC) injection and the structural formula of CX546. **b**, A representative time course showing the effects of CX546 on EPSC recordings. **c**,**d**, Summary data of EPSC peak amplitudes and decay times in ACC pyramidal neurons after CX546 perfusion ($n=8$ neurons from two mice. Peak and decay: Wilcoxon signed-rank test). **e**, Representative trace of three-chamber tests. **f**,**g**, Summary data of time spent in the social compartment and preference scores after administration of different doses of CX546 (WT-vehicle: $n=9$ mice; KO-vehicle: $n=6$ mice; KO + 5 mg: $n=6$ mice; KO + 10 mg: $n=9$ mice; KO + 20 mg: $n=8$ mice. Time and preference score: Kruskal–Wallis $H$-test with Nemenyi multiple comparisons test). **h**, Summary data of averaged total interaction time with a novel mouse after CX546 administration of different dosages (WT-vehicle: $n=8$ mice; KO-vehicle: $n=6$ mice; KO + 5 mg: $n=6$ mice; KO + 10 mg: $n=8$ mice; KO + 20 mg: $n=6$ mice. One-factor ANOVA with Tukey's multiple comparisons test). **i**, Representative traces of mEPSCs recorded in the ACC in the WT-vehicle, KO-vehicle and KO-10 mg CX546 groups. **j**, Summary data showing improvement in mEPSC frequencies and peak amplitudes after administration of 10 mg of CX546 (WT-vehicle: $n=12$ neurons from three mice; KO-vehicle: $n=12$ neurons from three mice; KO-CX546: $n=13$ neurons from three mice. Frequency: one-factor ANOVA with Tukey's multiple comparisons test; amplitude: Kruskal–Wallis $H$-test with Nemenyi multiple comparisons test). **k**, Representative traces of AMPAR/NMDAR-mediated EPSCs recorded in the ACC in the three groups. **l**, The AMPAR/NMDAR-mediated EPSC ratio was higher in the KO-CX546 group (WT-vehicle: $n=11$ neurons from three mice; KO-vehicle: $n=11$ neurons from four mice; KO-CX546: $n=14$ neurons from four mice. Kruskal–Wallis $H$-test with Nemenyi multiple comparisons test). **m**, Representative traces of AMPAR-mediated EPSCs. **n**, CX546 rescued AMPAR-mediated EPSCs (WT-vehicle: $n=13$ neurons from three mice; KO-vehicle: $n=18$ neurons from five mice; KO-CX546: $n=18$ neurons from four mice. Friedman's $M$-test). **o**, Representative traces of paired-pulse EPSCs. **p**, No difference was observed among the three groups (WT-vehicle: $n=12$ neurons from three mice; KO-vehicle: $n=14$ neurons from five mice; KO-CX546: $n=18$ neurons from four mice. Kruskal–Wallis $H$-test). Data are presented as the mean ± s.e.m. See Supplementary Table 2 for detailed statistical information. $^*P<0.05$, $^{**}P<0.01$, $^{****}P<0.0001$.

CX546 showed significantly enhanced mEPSCs, AMPA/NMDA ratio and input–output response than observed in slices of *Shank3* KO mice treated with vehicle (Fig. 7i–n). There was no difference in PPR between the *Shank3* KO mice treated with 10 mg kg$^{-1}$ CX546 and the WT or *Shank3* KO vehicle groups (Fig. 7o,p). These results corroborate the notion that ACC excitatory synapses have a critical role in social behaviors and may represent a new pharmacological intervention target for social dysfunction in ASD.

## Discussion

Our study provides direct evidence showing that *Shank3* deficiency leads to a loss of dendritic spines and impairments in AMPAR-mediated excitatory synaptic transmission and synaptic plasticity in ACC pyramidal neurons. The resulting hypoactivity in the pyramidal neurons of the ACC plays a causal role in the social interaction deficits observed in *Shank3* KO mice. Hence, the application of acute optogenetic or chemogenetic activation of pyramidal neurons in the ACC, the selective re-expression of *Shank3* in the ACC in adulthood or systemic administration of an AMPAR-positive modulator to boost excitatory synaptic transmission could improve social interaction in the global *Shank3* KO mouse model.

Previous clinical studies reported that anatomical structures in the ACC were altered and/or dysfunctional in ASD patients. For example, an examination of post-mortem brains from individuals with ASD found that the ACC appeared to be poorly laminated and to contain cells with reduced size[39]. Moreover, a neuroimaging study reported that glucose metabolism and volume of the right ACC were reduced in ASD patients[40]. Consistently, we found that ACC pyramidal neurons exhibited hypoactivity caused by reduced excitatory synaptic transmission and dendritic spine abnormality in *Shank3* KO mice. Although the ACC is known to have widespread connections with social information-encoding centers from both human and animal model studies[1,5], experimental evidence supporting a causal link between dysfunctional ACC and abnormal social behaviors is still lacking. Our study provides direct experimental evidence supporting that ACC dysfunction plays a causal role in social impairments in a mouse model of ASD with several approaches: first, we found that selective deletion of *Shank3* with CRISPR/Cas9 in the ACC mimicked the social deficits of the global *Shank3* KO mice; second, selective restoration of SHANK3 in the ACC ameliorated social deficits in the global *Shank3* KO mice and third, optogenetic or chemogenetic excitation of ACC pyramidal neuronal activity improved social interaction and social preference in the global *Shank3* KO mice.

Several studies have shown that the mPFC is highly relevant to social behavior, including social interaction, social dominance and social–spatial associations[27–30]. It is possible that the absence of *Shank3* in the mPFC plays a role in the impaired social behavior observed in global *Shank3* KO mice[23], which is worth exploring further in the future. Recent studies found that activation of mPFC could decrease social preference or produce social fear[27,41], whereas our present work showed that excitation of ACC increased social preference and social interaction. These results indicate that the mPFC and ACC may have distinct functions in social behavior. Further studies investigating the potential specific ACC and mPFC cell types and their functional interaction combined with real-time single-cell resolution imaging may clarify in more detail how the ACC and mPFC regulate social behaviors.

Besides the social function improvement, optogenetic activation of the ACC in this study induced an anxiolytic effect. Indeed, the ACC has been proposed to be involved in anxiety[42], and recent human studies have indicated a potential link between anxiety and social dysfunction[43]. It is possible that these two behavioral phenotypes may have, at least partially, shared underlying neural mechanisms. However, an intriguing observation is that photoinhibition to ACC neurons did not alter anxiety-related behaviors or locomotor behavior (Supplementary Fig. 16e). Such an observation is reminiscent of a recent report from Kang et al. showing that inhibiting excitatory neuronal activities in the ACC did not affect anxiety behaviors in a chronic pain model[44]. Moreover, when we restored *Shank3* or conditionally knocked out *Shank3* in ACC, we observed no significant changes in anxiety-like behavior. One possible explanation for the ACC's unidirectional regulation of anxiety may be that the anxiolytic effect relies on the activity of ACC under certain brain states, such as the 10 Hz optogenetic activation of the ACC pyramidal neurons in the current study, whereas the physiological range of ACC activity is not involved in anxiety generation and regulation. For the locomotor activity, we found that, although global *Shank3* KO mice displayed decreased total travel distance, CKO mice did not show motor deficits and also the CKI model did not rescue motor deficits. Excitation of ACC with ChR2 also did not affect locomotor behavior (data did not show here). These results demonstrate that absence of *Shank3* in ACC does not mediate the locomotor deficit seen in global *Shank3* KO mice.

Previous studies using different isoform-specific *Shank3* KO mouse lines have reported distinct changes in glutamate receptor subunit compositions and AMPA/NMDA ratio in different brain regions[16,17,45,46]. Consistently, we found that *Shank3* deletion induced AMPAR-mediated synaptic impairments in the ACC but not in the adjacent mPFC. Moreover, our previous study and another study on the ventral tegmental area found SHANK3 insufficiency produced distinct changes in different types of neuron in the same brain area[24,47]. The exact molecular mechanisms underlying these differential changes caused by *Shank3* deletion are still unknown, albeit with an array of evidences. One possibility is that the mPFC and the ACC may have differential transcriptome profiles[48], including different expression of many postsynaptic signaling proteins, which present different levels of compensation derived from other scaffold proteins after *Shank3* gene deletion. Alternatively, the mPFC and the ACC pyramidal neurons may have different isoforms of *Shank3* produced by different intragenic promoters and extensive alternative splicing[45]. In addition, we noticed that global KO, CKO and CKI of *Shank3* in the ACC showed slightly different component changes in glutamate receptors. One possible reason is that since the global *Shank3* KO is germline, there will be many compensatory changes throughout development, whereas CKO and CKI is done in adulthood, so any compensatory changes will likely be fewer and mechanistically different. Nevertheless, the functional alterations of AMPARs and the consistent AMPA/NMDA ratio are observed in all these models suggest that excitatory synaptic dysfunction in the ACC is one of the key phenotypes caused by *Shank3* mutation. In line with this notion, we found that chronic delivering CX546, an AMPAR PAM, could improve social behaviors in *Shank3* KO mice. Similar to our findings, Kim et al. found that Cntnap2 KO mice presented reduced AMPAR function and intraperitoneal administration of AMPAR PAM could specifically ameliorate social behavior without affecting the repetitive behavior[49]. These findings indicate that intervention on the convergent pathways and mechanisms of ASD may be a potential and feasible strategy for the treatment.

In the present work, we used several approaches, including optogenetics, DREADDs, adult restoration of *Shank3* and pharmacological strategies, to enhance the final output of ACC neurons through either excitability or synaptic transmission, thereby inducing improvements in social performance. Nevertheless, some of these results should be interpreted with caution. We noticed that a higher frequency of photostimulation seemed to have better effects than were observed for lower frequencies. However, if the stimulation was outside the physiological range of ACC neuronal activities, it is conceivable that the outcomes could be completely different because of disruptions in the excitatory/inhibition balance. Moreover, we observed that restoration of *Shank3* in adult mice resulted in relatively higher heterogeneity in the behavioral data.

Several factors could have contributed to behavioral heterogeneity, such as the possibility that Cre activity varied among different cells or those AAV-infected sub-regions within the ACC.

Overall, our study demonstrates that a causal link between ACC defects and social behavior in *Shank3* mutant mice by applying optogenetics, chemogenetics and pharmacological approaches. Future studies could aim to dissect the molecular and circuit-related mechanisms by which the ACC regulates social behavior, which would not only provide valuable insights into the neural substrates underlying social dysfunction characteristics to ASD but also help develop novel targeted therapeutics for ASD by tuning the ACC mediated circuit to correct the altered activity.

## Online content

Any methods, additional references, Nature Research reporting summaries, source data, statements of code and data availability and associated accession codes are available at https://doi.org/10.1038/s41593-019-0445-9.

Received: 9 February 2018; Accepted: 3 June 2019;
Published online: 22 July 2019

## References

1. Apps, M. A., Rushworth, M. F. & Chang, S. W. The anterior cingulate gyrus and social cognition: tracking the motivation of others. *Neuron* **90**, 692–707 (2016).
2. Dolen, G., Darvishzadeh, A., Huang, K. W. & Malenka, R. C. Social reward requires coordinated activity of nucleus accumbens oxytocin and serotonin. *Nature* **501**, 179–184 (2013).
3. Gunaydin, L. A. et al. Natural neural projection dynamics underlying social behavior. *Cell* **157**, 1535–1551 (2014).
4. Holroyd, C. B. & Yeung, N. Motivation of extended behaviors by anterior cingulate cortex. *Trends Cogn. Sci.* **16**, 122–128 (2012).
5. Chang, S. W., Gariépy, J. F. & Platt, M. L. Neuronal reference frames for social decisions in primate frontal cortex. *Nat. Neurosci.* **16**, 243–250 (2012).
6. Willsey, A. J. & State, M. W. Autism spectrum disorders: from genes to neurobiology. *Curr. Opin. Neurobiol.* **30**, 92–99 (2015).
7. Bourgeron, T. Current knowledge on the genetics of autism and propositions for future research. *C. R. Biol.* **339**, 300–307 (2016).
8. Durand, C. et al. Mutations in the gene encoding the synaptic scaffolding protein SHANK3 are associated with autism spectrum disorders. *Nat. Genet.* **39**, 25–27 (2007).
9. Moessner, R. et al. Contribution of SHANK3 mutations to autism spectrum disorder. *Am. J. Hum. Genet.* **81**, 1289–1297 (2007).
10. Gauthier, J. et al. Novel de novo SHANK3 mutation in autistic patients. *Am. J. Med. Genet. B* **150B**, 421–424 (2009).
11. Naisbitt, S. et al. Shank, a novel family of postsynaptic density proteins that binds to the NMDA receptor/PSD-95/GKAP complex and cortactin. *Neuron* **23**, 569–582 (1999).
12. Sala, C. et al. Regulation of dendritic spine morphology and synaptic function by Shank and Homer. *Neuron* **31**, 115–130 (2001).
13. Monteiro, P. & Feng, G. SHANK proteins: roles at the synapse and in autism spectrum disorder. *Nat. Rev. Neurosci.* **18**, 147–157 (2017).
14. Bozdagi, O. et al. Haploinsufficiency of the autism-associated Shank3 gene leads to deficits in synaptic function, social interaction, and social communication. *Mol. Autism* **1**, 15 (2010).
15. Peça, J. et al. Shank3 mutant mice display autistic-like behaviours and striatal dysfunction. *Nature* **472**, 437–442 (2011).
16. Wang, X. et al. Synaptic dysfunction and abnormal behaviors in mice lacking major isoforms of Shank3. *Hum. Mol. Genet* **20**, 3093–3108 (2011).
17. Kouser, M. et al. Loss of predominant Shank3 isoforms results in hippocampus-dependent impairments in behavior and synaptic transmission. *J. Neurosci.* **33**, 18448–18468 (2013).
18. Lee, J. et al. Shank3-mutant mice lacking exon 9 show altered excitation/inhibition balance, enhanced rearing, and spatial memory deficit. *Front. Cell Neurosci.* **9**, 94 (2015).
19. Speed, H. E. et al. Autism-associated insertion mutation (InsG) of Shank3 Exon 21 causes impaired synaptic transmission and behavioral deficits. *J. Neurosci.* **35**, 9648–9665 (2015).
20. Jaramillo, T. C. et al. Altered striatal synaptic function and abnormal behaviour in Shank3 Exon4-9 deletion mouse model of autism. *Autism Res.* **9**, 350–375 (2016).
21. Mei, Y. et al. Adult restoration of Shank3 expression rescues selective autistic-like phenotypes. *Nature* **530**, 481–484 (2016).
22. Wang, X. et al. Altered mGluR5-Homer scaffolds and corticostriatal connectivity in a Shank3 complete knockout model of autism. *Nat. Commun.* **7**, 11459 (2016).
23. Zhou, Y. et al. Mice with Shank3 mutations associated with ASD and schizophrenia display both shared and distinct defects. *Neuron* **89**, 147–162 (2016).
24. Wang, W. et al. Striatopallidal dysfunction underlies repetitive behavior in Shank3-deficient model of autism. *J. Clin. Investig.* **127**, 1978–1990 (2017).
25. Rudebeck, P. H., Buckley, M. J., Walton, M. E. & Rushworth, M. F. A role for the macaque anterior cingulate gyrus in social valuation. *Science* **313**, 1310–1312 (2006).
26. Behrens, T. E., Hunt, L. T., Woolrich, M. W. & Rushworth, M. F. Associative learning of social value. *Nature* **456**, 245–249 (2008).
27. Murugan, M. et al. Combined social and spatial coding in a descending projection from the prefrontal cortex. *Cell* **171**, 1663–1677.e1616 (2017).
28. Zhou, T. et al. History of winning remodels thalamo-PFC circuit to reinforce social dominance. *Science* **357**, 162–168 (2017).
29. Ferguson, B. R. & Gao, W. J. Thalamic control of cognition and social behavior via regulation of gamma-aminobutyric acidergic signaling and excitation/inhibition balance in the medial prefrontal cortex. *Biol. Psychiatry* **83**, 657–669 (2018).
30. Benekareddy, M. et al. Identification of a corticohabenular circuit regulating socially directed behavior. *Biol. Psychiatry* **83**, 607–617 (2017).
31. Bourgeron, T. A synaptic trek to autism. *Curr. Opin. Neurobiol.* **19**, 231–234 (2009).
32. Zhang, Q. et al. Impaired dendritic development and memory in sorbs2 knock-out mice. *J. Neurosci.* **36**, 2247–2260 (2016).
33. Jia, F., Miao, H., Zhu, X. & Xu, F. Pseudo-typed Semliki Forest virus delivers EGFP into neurons. *J. Neurovirol.* **23**, 205–215 (2017).
34. Toyoda, H. et al. Roles of the AMPA receptor subunit GluA1 but not GluA2 in synaptic potentiation and activation of ERK in the anterior cingulate cortex. *Mol. Pain.* **5**, 46 (2009).
35. Ran, F. A. et al. In vivo genome editing using *Staphylococcus aureus* Cas9. *Nature* **520**, 186–191 (2015).
36. Allsop, S. A. et al. Corticoamygdala transfer of socially derived information gates observational learning. *Cell* **173**, 1329–1342.e1318 (2018).
37. Lauterborn, J. C., Lynch, G., Vanderklish, P., Arai, A. & Gall, C. M. Positive modulation of AMPA receptors increases neurotrophin expression by hippocampal and cortical neurons. *J. Neurosci.* **20**, 8–21 (2000).
38. Lipina, T., Weiss, K. & Roder, J. The ampakine CX546 restores the prepulse inhibition and latent inhibition deficits in mGluR5-deficient mice. *Neuropsychopharmacol.* **32**, 745–756 (2007).
39. Simms, M. L., Kemper, T. L., Timbie, C. M., Bauman, M. L. & Blatt, G. J. The anterior cingulate cortex in autism: heterogeneity of qualitative and quantitative cytoarchitectonic features suggests possible subgroups. *Acta Neuropathol.* **118**, 673–684 (2009).
40. Haznedar, M. M. et al. Limbic circuitry in patients with autism spectrum disorders studied with positron emission tomography and magnetic resonance imaging. *Am. J. Psychiatry* **157**, 1994–2001 (2000).
41. Xu, H. et al. A disinhibitory microcircuit mediates conditioned social fear in the prefrontal cortex. *Neuron* **102**, 668–682.e5 (2019).
42. Etkin, A., Prater, K. E., Hoeft, F., Menon, V. & Schatzberg, A. F. Failure of anterior cingulate activation and connectivity with the amygdala during implicit regulation of emotional processing in generalized anxiety disorder. *Am. J. Psychiatry* **167**, 545–554 (2010).
43. White, S. W., Oswald, D., Ollendick, T. & Scahill, L. Anxiety in children and adolescents with autism spectrum disorders. *Clin. Psychol. Rev.* **29**, 216–229 (2009).
44. Kang, S. J. et al. Bidirectional modulation of hyperalgesia via the specific control of excitatory and inhibitory neuronal activity in the ACC. *Mol. Brain* **8**, 81 (2015).
45. Wang, X., Xu, Q., Bey, A. L., Lee, Y. & Jiang, Y. H. Transcriptional and functional complexity of Shank3 provides a molecular framework to understand the phenotypic heterogeneity of SHANK3 causing autism and Shank3 mutant mice. *Mol. Autism* **5**, 30 (2014).
46. Bey, A. L. et al. Brain region-specific disruption of Shank3 in mice reveals a dissociation for cortical and striatal circuits in autism-related behaviors. *Transl. Psychiatry* **8**, 94 (2018).
47. Bariselli, S. et al. SHANK3 controls maturation of social reward circuits in the VTA. *Nat. Neurosci.* **19**, 926–934 (2016).
48. Forero, D. A., Guio-Vega, G. P. & Gonzalez-Giraldo, Y. A comprehensive regional analysis of genome-wide expression profiles for major depressive disorder. *J. Affect. Disord.* **218**, 86–92 (2017).
49. Kim, J. W. et al. Pharmacological modulation of AMPA receptor rescues social impairments in animal models of autism. *Neuropsychopharmacol.* **44**, 314–323 (2018).

## Acknowledgements

We thank J. Kang, M. Wang, X. Wang, T. Luo, Y. Lu, X. Wei (Fourth Military Medical University), D. Wang, X. Gao, M. Fleishman (McGovern Institute for Brain Research, Massachusetts Institute of Technology), Z. Fan and D. Zheng (Zhejiang University) for technical support and suggestions. We thank H. Dong (University of Southern California) for suggestions on the anatomical specificity test, and X. Zhang (University of Ottawa) for critical reading and discussions. We thank L. Shang (Fourth Military Medical University) for suggestions on data statistics. We thank Y. Wu for supporting us during schematic drawing. This study was supported by the Natural Science Foundation of China (nos. 81730035 to S.W., 81771476 and 81371498 to W.W.), Innovation Teams in Priority Areas Accredited by the Ministry of Science and Technology (no. 2014RA4029, S.W.), the International Science and Technology Cooperation Program of China (no. 2011DFA32560, S.W.) and NIMH grant no. MH097104 and P50MH094271 (G.F.). We also thank the Nature Research Editing Service for English language editing (certificate verification key 8862-92CC-FDBE-B0BA-035P).

## Author contributions

B.G., G.F., W.W. and S.W. designed the experiments. B.G. performed in vitro patch-clamp recording. J.C. and J.Y. performed the fluorescence in situ hybridization and immunohistochemistry. B.G. and J.C. conducted the fiber photometry and behavior test. Q.C. designed the Cas9 gRNA. B.G. and Q.C. performed in vivo optrode recording. B.G., K.R., H.Y. and C.Q. performed the viral injection and behavioral test. B.G., Q.C., H.L. and T.L.-J. conducted the pharmacological rescue experiments. B.G. and D.F. performed the western blot. B.G., Q.C. and F.J. performed sparse labeling and morphological characterization analyses. Y.L. conducted the electron microscopy. H.M. performed statistical analyses. G.F., W.W. and S.W. wrote the paper with the assistance of B.G., J.C., Q.C., H.H. and Z.F.

## Competing interests

The authors declare no competing interests.

## Additional information

**Supplementary information** is available for this paper at https://doi.org/10.1038/s41593-019-0445-9.

**Reprints and permissions information** is available at www.nature.com/reprints.

**Correspondence and requests for materials** should be addressed to G.F., W.W. or S.W.

**Peer review information:** *Nature Neuroscience* thanks Camilla Bellone and the other anonymous reviewer(s) for their contribution to the peer review of this work.

**Publisher's note:** Springer Nature remains neutral with regard to jurisdictional claims in published maps and institutional affiliations.

## Methods

**Animals.** All procedures were approved by the Institutional Animal Care and Use Committee of the Fourth Military Medical University (FMMU) and conformed to the Guide for the Care and Use of Laboratory Animals published by the National Institutes of Health (NIH). Mice were housed in a room maintained at a constant temperature and on a 12-h light/dark cycle (light from 08:00 to 20:00). Water and food were available ad libitum. All animals were randomly allocated to the different experimental conditions used in this study. The *Shank3B*$^{-/-}$, CKI (*Shank3*$^{fx/fx}$) and Thy1-GCaMP3 mouse strains have been previously characterized[15,21,50], and all mice had a pure C57BL/6J background. Male and female mice aged 2–6 months old were used in the electrophysiological experiments. All virus injections were administered to mice aged 2–3 months old. All experiments were performed in age-matched mixed gender mice by experimenters blinded to the genotypes and groups.

**Viral vectors.** pAAV-CaMKIIa-hChR2(H134R)-EYFP (Addgene plasmid no. 26969) was a gift from K. Deisseroth, and pAAV-EF1a-DIO-hM3D(Gq)-mCherry (Addgene plasmid no. 50460) was a gift from B. Roth; both vectors were serotyped with AAV2/8 and packaged by Obio Technology. AAV2/8-CaMKIIa-EYFP and AAV2/8-CaMKIIa-Cre-EGFP were reconstructed and tested by Obio Technology, and the viral titer was (2–5)×10$^{12}$ particles per ml. The use of AAV was approved by the above-named institutional committees. SFV-EGFP was provided by BrainVTA. All viral vectors were aliquoted and stored at −80 °C until used.

**SaCas9 plasmid construction and AAV vector production.** To minimize off-target effects, three guide RNAs (gRNA1: GGGCTATTCCAGCCTCCCTCC; gRNA2: GGCAGGGGCGTGTCCAGGTTAG; gRNA3: TTGGCGGCCCACACG GGCGCGG) corresponding to SHANK3 were designed using the CRISPR design tool (http://www.rgenome.net/cas-designer/) and cloned into pX601-AAV-CMV::NLS-SaCas9-NLS-3xHA-bGHpA;U6::BsaI-sgRNA (abbreviated pX601; Addgene plasmid no. 61591), a gift from F. Zhang[35]. The gRNAs were designed and confirmed by sequencing in HanBio Technology. Then the plasmid was modified with 2A-GFP by TIANYI HUIYUN. After the plasmids were confirmed by sequencing, we transfected those constructs into N2A mouse cells. A T7E1 assay was performed to evaluate indel efficiency at 72 h after transduction. We then chose gRNA2, which had the best efficiency, to package in AAV serotype 8 (PackGene Biotech) for administration to the mice.

**Stereotaxic surgery.** Mice were anesthetized with isoflurane (4% for induction and 1.5% thereafter for maintenance), and their heads were fixed in a stereotaxic injection frame (RWD Life Science Inc.). All skull measurements were made relative to Bregma, and viral injection into the ACC was performed using a microinjection needle with a 10-μl microsyringe (Gaoge) to deliver the virus at a rate of 50 nl min$^{-1}$ using a microsyringe pump (Kd Scientific). Following viral injection, the needle was held at the site for 10 min to allow diffusion of the virus. The stereotaxic coordinates for ACC injection were anterior posterior (AP) 1.00, medial lateral (ML) 0.35 and dorsal ventral (DV) 2.00 mm. For optical activation behavioral experiments, 350 nl of AAV2/8-CaMKIIa-ChR2-EYFP, AAV2/8-CaMKIIa-eNpHR3.0-EYFP or AAV2/8-CaMKIIa-EYFP was unilaterally injected into the ACC, and optical fibers (230 μm optical density (OD), 0.37 numerical aperture (NA), Thorlabs) were implanted in the ipsilateral ACC. For the DREADDs activation behavioral experiments, a 350-nl mixture of AAV2/8-CaMKIIa-Cre-EGFP and AAV2/8-EF1a-DIO-hM3D(Gq)-mCherry or AAV2/8-CaMKIIa-EYFP and AAV2/8-EF1a-DIO-hM3D(Gq)—mCherry was unilaterally injected into the ACC. For the conditional knockout and rescue experiments, 300 nl of AAV2/9-SaCas9-GFP or AAV2/8-CaMKIIa-Cre-EGFP was bilaterally injected into the ACC. Data were excluded only in experiments where viral injections were performed and post hoc analysis of viral targeting demonstrated that injections were inaccurate.

**Behavioral tests and in vivo optogenetic manipulations.** For optical stimulation during behavioral tests, the laser was connected to a patch cord, which was connected through a fiber-optic rotary joint allowing free rotation of the fiber. The optogenetic manipulation protocol was performed as previously reported[3]. Mice were connected to the patch cable and then allowed to recover from handling for 1–3 min before the 15-min test was initiated. The 15-min test was divided into three 5-min epochs: laser stimulation off, on and off (OFF-ON-OFF epochs). Photoactivation of ACC cell bodies was induced by 10-Hz light trains with 5-ms pulses of blue light generated by a 473-nm diode-pumped solid-state laser. For the experiment performed to compare the effects of different photostimulation patterns, mice were randomized to receive 5, 10 or 20 Hz of stimulation in each epoch with a between-epoch interval time of 30 min. Photoinhibition of ACC cell bodies was induced by applying constant yellow light generated by a 594-nm diode-pumped solid-state laser.

**Anxiety-like behaviors.** All tests were performed during the dark phase, and the animals were allowed to acclimatize to the behavioral testing room for 1 d. The elevated plus maze test was performed in a maze consisting of two open arms (30×5×30 cm$^3$) and two enclosed arms (30×5×30 cm$^3$) that extended from a central platform (5×5 cm$^2$) at 90°. The open field chamber was a 50×50×40 cm$^3$ box, and mice were introduced into a corner at the start of the test. The parameters measured included the time spent and distance traveled in the central area and the total distance moved. The marble-burying test was performed in a clean cage (29×18×15 cm$^3$) that was filled to approximately 5 cm deep with wood-chip bedding that was lightly tamped down to make a flat surface. Next, 20 glass marbles were placed in a regular pattern on the surface and spaced approximately 4 cm from each other. Each mouse remained in the cage for 30 min. Another experimenter blind to the experimental conditions counted the number of marbles buried (to two-thirds their depth) in the bedding. For the one-chamber novel object task, a novel object was placed in an open chamber (50×50×40 cm$^3$), and each mouse was introduced into one corner of the chamber. The time spent exploring the region of the object was analyzed using SMART v.3.0 software. In the four-chamber novel object task, an open chamber (50×50×40 cm$^3$) was divided into four zones and distinct novel objects were placed in the center of each zone. Mice were introduced to the center of the chamber and allowed to explore freely. The activity of the mouse was video-recorded, and the zone crossings were analyzed using SMART v.3.0 software (Panlab Harvard Apparatus).

**Social interaction in the home cage.** Mice were allowed to explore the home cage freely for 1 min (habituation) before an unfamiliar juvenile male mouse (3–4 weeks old) was introduced into the cage. Measured social interaction behaviors included body sniffing, anogenital sniffing, direct contact and close following (<1 cm) initiated by the test mouse. All behaviors were video-recorded and analyzed using SMART v.3.0 software by experimenters who were blind to the testing conditions.

**Three-chamber sociability test.** The test apparatus consisted of three chambers: a middle chamber (40×20 cm$^2$) and another two chambers (40×20 cm$^2$) in which wire cages containing stranger mice were placed. For the sociability test, the test animal was placed in the middle chamber for 5 min to habituate. Then, a wire cage containing a novel juvenile male mouse was placed in one of the side chamber, and an empty wire cage was placed in the other. The time spent in each chamber and the time spent in close proximity to the wire cages were analyzed using SMART v.3.0 software.

**Grooming behaviors.** Grooming behaviors were measured as described previously[24]. In brief, to measure basal grooming behavior, we video-recorded mice in the dark phase for 1 or 2 h. The measured grooming behaviors included face wiping, scratching/rubbing of head and ears and full-body grooming. After recording the behaviors, the experimenters were blinded to the genotypes and manually analyzed the videotapes.

**Pharmacological rescue experiments.** For the AMPAR modulator treatment experiments, *Shank3* KO mice were randomly subcutaneously injected with CX546 (Tocris no. 2980, in 1% DMSO) at 5, 10 or 20 mg kg$^{-1}$ or with vehicle for 7 d. After treatment, we performed either behavioral assessments or electrophysiological tests. For CX546 infusion in ACC, surgery was performed as described previously[51]. Bilateral 26 gauge (Ga) stainless steel guide cannula (0.8 mm separation, RWD Life Science) were implanted into the ACC according to the above coordinates and were secured to the skull with dental cement. The removable obturators (33 Ga OD) at the full length of the guide cannulae were inserted into the guide cannula to limit obstruction. After surgery, animals were housed separately and given 5–7 d of recovery time. Microinjection was performed 30 min before behavioral tests. Mice were lightly restrained and obturators were removed. Sterile 33 Ga microinjection needles were connected to two 10 μl syringes (Hamilton) via PE-50 tubing. Microinjection needles were inserted bilaterally to a depth 0.5 mm beyond the ventral tip of the guide cannula. CX546 solution was resuspended in 0.9% saline to concentration of 400 μM and was infused in a volume of 500 nl per side over a 2 min period. Then, the microinjection needles remained in place for additional 1 min for drug diffusion. After the diffusion, the injector was removed and the obturators were replaced.

**DREADDs rescue experiments.** For the DREADDs rescue experiments, CNO was administered 3 weeks after AAV2/8-EF1a-DIO-hM3D (Gq) injection. To test the effect of CNO, the mice were placed in a new clean cage for 30 min to habituate before basal grooming behaviors were recorded for 1 h. The mice were injected with 0.7 mg kg$^{-1}$ CNO and then immediately transferred back to the recording cages where recording was initiated after 30 min. For social behaviors, mice were injected with CNO 30 min before receiving the social interaction test in their home cage. Then, the juvenile mice were removed and left in the home cage for 30 min to habituate, and the three-chamber test was performed.

**Fiber photometry.** Fiber photometry was used to record calcium signals using a commercialized fiber photometry system (ThinkerTech) as described previously[52]. Using Thy1-GCaMP3 mice, we planted an optical fiber (230 μm OD, 0.37 NA; Thorlabs) into the ACC (AP: 1.00 mm; ML: 0.35 mm; DV: 1.90 mm). We used a skull-penetrating M1 screw and dental acrylic to support the ceramic ferrule. To record the fluorescence signals, a 488-nm laser beam (OBIS 488LS; Coherent) was reflected off a dichroic mirror (MD498, Thorlabs) that was focused by a

×10 objective lens (0.3 NA; Olympus) and coupled to an optical commutator (Doris Lenses). An optical fiber (230 µm OD, 0.37 NA) guided the light between the commutator and the implanted optical fiber. The laser power at the tip of the optical fiber was adjusted to 0.01–0.02 mW to decrease laser bleaching. Fluorescence was bandpass-filtered (MF525-39, Thorlabs), and an amplifier was used to convert the photomultiplier tube current output to a voltage signal. The analog voltage signals were digitalized at 500 Hz and recorded by a Power 1401 digitizer with Spike2 software (CED).

**In vitro electrophysiology.** Whole-cell patch-clamp recording was performed as described previously[51]. Briefly, the mice were anesthetized with isoflurane and transcardially perfused with ice-cold carbogenated (95% $O_2$, 5% $CO_2$) cutting solution containing the following: 115 mM choline chloride, 2.5 mM KCl, 1.25 mM $NaH_2PO_4$, 0.5 mM $CaCl_2$, 8 mM $MgCl_2$, 26 mM $NaHCO_3$, 10 mM D-(+)-glucose, 0.1 mM L-ascorbic acid and 0.4 mM sodium pyruvate (300–305 mOsm $l^{-1}$). Coronal slices (300 µm-thick) containing the ACC (bregma 1.42 to 0.50 mm, determined by the shapes of lateral ventricles and corpus callosum) were prepared using a vibratome (VT1200S, Leica). Whole-cell patch-clamp recordings were made using infrared differential interference contrast visualization at 28–30 °C in artificial cerebral spinal fluid (ACSF) containing the following: 119 mM NaCl, 2.3 mM KCl, 1.0 mM $NaH_2PO_4$, 26 mM $NaHCO_3$, 11 mM D-(+)-glucose, 1.3 mM $MgSO_4$ and 2.5 mM $CaCl_2$ (pH 7.4, 295–300 mOsm $l^{-1}$). Patch pipettes were filled with a solution containing the following: 128 mM potassium gluconate, 10 mM HEPES, 10 mM phosphocreatine sodium salt, 5 mM lidocaine *N*-ethyl chloride, 1.1 mM EGTA, 5 mM ATP magnesium salt and 0.4 mM GTP sodium salt (pH 7.3, 300–305 mOsm $l^{-1}$). The recordings were obtained using a multiclamp 700B amplifier (Molecular Devices) filtered at 5 kHz and sampled at 20 kHz with a Digidata 1550B. Clampex 10.7 was used for acquisition and analysis. Data were excluded when the resting membrane potential of neurons were positive than −60 mV and action potentials did not have overshoot.

**mEPSCs.** The cell membrane potential was clamped at −70 mV in the presence of 50 µM DL-2-amino-5-phosphonovaleric acid (APV), 25 µM 1(*S*),9(*R*)-(−)-bicuculline methobromide (BMR) and 1 µM tetrodotoxin (all three drugs from Tocris). The mEPSCs were detected and analyzed using Mini Analysis (Synaptosoft Inc.).

**PPR.** The cell membrane potential was held at −70 mV, and monosynaptic EPSCs were evoked with a bipolar platinum electrode placed in layer V/VI of the cortex. Recordings were made in the presence of 50 µM APV and 25 µM BMR, and the stimulation was current-controlled (ISO-Flex, AMPI). The paired stimuli were delivered at an inter-stimulus interval of 50 ms. The PPR was calculated as the peak current response to the second pulse divided by that to the first pulse.

**Input–output.** To measure the input–output response of AMPAR-mediated EPSCs, the cell membrane potential was held at −70 mV and recording was performed in the presence of 50 µM APV and 25 µM BMR. The NMDAR-mediated EPSC input-output response was recorded in $Mg^{2+}$-free ACSF, and the cells were held at −70 mV in the presence of 50 µM NBQX and 25 µM BMR. The stimulus intensity was set as a step from 0.1 to 1 mA, and the recording electrode and stimulus electrode were kept at a relatively fixed distance.

**AMPAR/NMDAR ratio.** The AMPAR- and NMDAR-mediated current ratio was recorded in the presence of 25 µM BMR at holding membrane potentials of −70 mV and +40 mV with an internal solution containing the following: 107 mM $CsMeSO_3$, 10 mM CsCl, 3.7 mM NaCl, 5 mM TEA-Cl, 20 mM HEPES, 0.2 mM EGTA, 5 mM lidocaine *N*-ethyl chloride, 4 mM ATP magnesium salt, 0.3 mM GTP sodium salt and 2 mM $MgCl_2$. The pH was adjusted to 7.3 with KOH, and osmolarity was adjusted to 298–300 mOsm with 15 mM $K_2SO_4$ (~8–10 mM). The AMPAR/NMDAR ratio was calculated as the ratio of the average EPSC peak amplitude at −70 mV to the average amplitude of EPSCs recorded at +40 mV (average of 40–50 ms after afferent stimulation).

**LTP.** In the ACC, LTP recording was performed as described previously[34,53]. Briefly, we recorded EPSCs from neurons in layers II/III with the stimulus electrode placed in layer V/VI. LTP was induced by eight paired presynaptic pulses at 2 Hz coupled with postsynaptic depolarization at + 30 mV. Data were excluded when the series resistance changed by >20%.

**Intrinsic membrane properties.** To measure the intrinsic membrane properties of ACC neurons, whole-cell recordings were carried out in current-clamp mode at −60 mV, and spikes were induced by incrementally increasing the current injection (each step increase was 20 pA). The recordings were obtained in the presence of 50 µM APV, 50 µM NBQX and 25 µM BMR to block the synaptic inputs.

**In vivo recording.** Optical-tagging in vivo recording was performed with a multichannel neural data acquisition system (OmniPlex, Plexon). Mice were implanted with a 16-channel optrode (MW-TE-16-2×2, *PLEXON*) that targeted the ACC via a procedure similar to that used in an optical fiber implant. The mice were housed singly for 1–2 weeks during recovery from surgery, and they wore the wire connected to the optrodes to habituate to them during this period. The recording method and analysis were performed in a manner consistent with previous reports. After the optrode was connected with the amplifier, we recorded wide band signals (0.5–8,000 Hz) with amplification (×20,000 gain) and digitized the data at 40 kHz in the ACC. The raw signals were filtered (250–8,000 Hz) to remove the local field potential signals. We delivered different stimulation patterns (5, 10 or 20 Hz) for 10 s during the recording while the mice were freely moving in their home cage. Single-unit spike sorting was performed by Off-Line Spike Sorter (v.4.0, Plexon) and analyzed with NeuroExplorer 5.0 (Plexon). All animals used in the in vivo recording experiments were perfused after recording, and the positions of the recording sites were verified.

**Sparse labeling and morphological characterization analyses.** To sparsely label pyramidal neurons in the ACC, we adopted two types of virus-based method. In the AAV-based method, 50 µl of AAV9-hSyn-EGFP-P2A-EGFPf virus[24] was delivered into the mouse blood circulation through a retroorbital injection into the venous sinus at a viral titer of $5\times10^{11}$ GC per ml. The mice were euthanized 3 weeks after virus injection. In the SFV-based method, 500 nl of SFV-EGFP virus[33,54] was stereotaxically microinjected into the ACC at a titer of $2.1\times10^{6}$ (PFU per ml). After 12 h, the mice were euthanized. The coronal slices (200 µm) containing the ACC were PFA-fixed and immunostained with an anti-GFP antibody (Invitrogen A11122) to enhance EGFP expression. The images were captured using an FV1200 confocal microscope (Olympus, Japan), and Imaris software (v.7.7.1, Bitplane) was used to reconstruct neuronal dendritic arbors and dendritic spines. Dendritic length, branching complexity and branch-point locations in a series of concentric circles (at 10-µm radius increments from the soma) throughout the whole dendritic arbor were quantified for the Sholl analysis. A dendritic spine analysis was performed semi-automatically using confocal *Z*-stack images, and we analyzed spines that were 30–50 µm away from the outer edge of the soma and extending for an additional 10–60 µm away from the starting point. The images were visualized in Imaris software, and reconstructed dendritic spines were recognized automatically. An observer blinded to the experimental groups manually edited the reconstructions to include or exclude misidentified spines. Spine classification was then completed in the Imaris spine classification module.

**In situ hybridization histochemistry.** The mice were deeply anesthetized with isoflurane and transcardially perfused with 30 ml of 0.01 M diethylpyrocarbonate-treated phosphate-buffered saline (DEPC–PBS, pH 7.4) followed by 100 ml of 4% (w/v) formaldehyde in 0.1 M phosphate buffer (pH 7.4). The brains were removed and postfixed with the same fixative for 2 d at 4 °C. After they were cryoprotected in 30% (w/v) sucrose in 0.1 M DEPC–PBS at 4 °C overnight, the brains were cut into 30 µm-thick coronal sections on a freezing microtome.

A complementary DNA fagment of vesicular glutamate transporter 1 (VGLUT1, nucleotides 152-1085, GenBank accession no. NM_182993.2) or *Shank3* (nucleotides 3445–4128; GenBank accession no. NM_021423.3) was cloned into the pCR II-TOPO vector (Invitrogen 450640). Using the linearized plasmids as a template, we synthesized sense and antisense single-strand riboprobes with a digoxigenin (DIG) RNA labeling kit (Roche 11277073910, Roche Diagnostics) and an in vitro transcription kit (MEGAscrip T7/SP6, Invitrogen AM1322). Free-floating sections were incubated at room temperature for 10 min in 2% (v/v) $H_2O_2$ in 0.1 M DEPC–PBS and then treated with 0.3% (v/v) Triton X-100 in 0.1 M DEPC–PBS for 20 min. After that, the sections were acetylated for 10 min in freshly prepared 0.25% (v/v) acetic anhydride in 0.1 M triethanolamine. After two rinses in DEPC–PBS, the sections were pre-incubated for 1 h at 58 °C with a hybridization buffer composed of 50% (v/v) formamide, 5× sodium citrate (SSC), 2% (w/v) blocking reagent, 0.1% (w/v) *N*-lauroylsarcosine (NLS) and 0.1% (v/v) sodium lauryl sulfate. The sections were then hybridized for 16–18 h at 58 °C with 1 µg $ml^{-1}$ sense or antisense DIG-labeled VGLUT1 or *Shank3* riboprobes in hybridization buffer. After two 20-min washes at 58 °C in 50% (v/v) formamide, 2× SSC and 0.1% (w/v) NLS, the hybridized sections were treated for 30 min at 37 °C with 10 µg $ml^{-1}$ RNase A (Toyobo) in 10 mM Tris–HCl (pH 8.0), 1 mM EDTA and 0.5 M NaCl. The sections were washed at 37 °C twice for 10 min each in 2× SSC and 0.1% (w/v) NLS and then twice for 10 min each in 0.2× SSC and 0.1% (w/v) NLS. The following incubations were performed at room temperature in 1% (w/v) blocking reagent in 0.1 M Tris–HCl (pH 7.5) and 0.15 M NaCl. After a wash, the hybridized sections were incubated overnight at room temperature in a mixture of peroxidase-conjugated anti-digoxigenin antibody (Roche 11207733910) diluted 1:2,000 and one of the following antibodies: goat anti-GFP antibodies (1:800, Rockland 600101215), rabbit anti-NeuN antibodies (1:500, Millipore ABN78), mouse anti-GFAP antibodies (1:1,000, Sigma SAB1405864), goat anti-Iba1 antibodies (1:200, Abcam ab5076), mouse anti-CaMKII antibodies (1:200, Abcam ab22609) or mouse anti-GAD67 antibodies (1:1,000, Millipore MAB5406). To amplify the signals for the VGLUT1 or *Shank3* mRNAs, we performed biotinylated tyramine-glucose oxidase amplification[55]. After washing, the sections were incubated for 3–4 h in a mixture of 2 µg $ml^{-1}$ Alexa Fluor 488-conjugated streptavidin to visualize the riboprobes (Invitrogen) and 4 µg $ml^{-1}$ Alexa Fluor 594-conjugated anti-mouse, anti-rabbit or anti-goat IgG to visualize other molecules (Invitrogen). After double labeling, all sections were incubated with DAPI (1:5,000; Molecular Probes)

for 5 min at room temperature. The sections were air-dried and cover-slipped with a mixture of 50% (v/v) glycerol and 2.5% (w/v) triethylenediamine in 0.01 M PBS.

**Immunofluorescence histochemistry.** The mice were deeply anesthetized with isoflurane and transcardially perfused with 30 ml of 0.01 M PBS (pH 7.4) followed by 100 ml of 4% (w/v) formaldehyde in 0.1 M phosphate buffer (pH 7.4). The brains were removed and postfixed with the same fixative for 4 h at 4 °C. After cryoprotection with 30% (w/v) sucrose in 0.1 M phosphate buffer at 4 °C overnight, the brains were cut into 30 µm-thick frontal sections on a freezing microtome. The sections were incubated overnight at room temperature with mouse anti-SHANK3 antibodies (1:200, NeuroMab 75344). After the sections were washed, they were incubated for 3–4 h with 4 µg ml$^{-1}$ Alexa Fluor 594-conjugated anti-mouse IgG (Invitrogen) to visualize SHANK3. Finally, the sections were air-dried and cover-slipped with a mixture of 50% (v/v) glycerol and 2.5% (w/v) triethylenediamine in 0.01 M PBS.

**Western blot analysis.** Western blotting was performed as described previously[51]. Briefly, ACC tissues were collected after coronal dissection and lysed in RIPA lysis buffer (10 mM Tris, 150 mM NaCl, 1% Triton X-100, 0.5% NP-40 and 1 mM EDTA at pH 7.4) containing a 1:100 (v/v) ratio of protease and phosphatase inhibitor cocktail (Roche). The protein samples were quantified using a bicinchoninic acid assay, resolved via sodium dodecyl sulfate-polyacrylamide gel electrophoresis (SDS–PAGE), and transferred to polyvinylidene difluoride membranes. Primary antibodies against the following targets were used: SHANK3 (Santa Cruz, SC-30193), GluR1 (Abcam, ab31232), GluR2 (Abcam, ab20673), NR1 (Abcam, EPR2481), NR2A (Abcam, EPR2465), NR2B (Abcam, ab65783) and β-actin (Cell Signalling Technology, 3700). Proteins were visualized using the enhanced chemiluminescence detection method (Advansta). The scanned images were quantified using ImageJ software. Specific bands were then quantified and normalized to β-actin loading control for each lane and each blot.

**Electron microscopy.** Mice were deeply anesthetized with isoflurane and transcardially perfused with PBS (pH 7.4) followed by 500 ml of an ice-cold mixture of 4% paraformaldehyde and 0.05% glutaraldehyde in 0.1 M phosphate buffer (pH 7.4) over 2 h. Coronal slices containing the ACC were dissected, placed in 1% osmium tetroxide in 0.1 M phosphate buffer for 1.5 h, dehydrated in a graded ethanol series and propylene oxide and flat-embedded in Epon 812 (SPI-Chem). Ultrathin sections were cut with an ultramicrotome (EM UC6, Leica), mounted on mesh grids (6–8 sections per grid), counter-stained with uranyl acetate and lead citrate and observed under a JEM-1230 electron microscope (JEOL Ltd). Electron micrographs were captured with a Gatan digital camera and its application software (832 SC1000). Postsynaptic densities were measured using ImageJ (NIH) by observers blinded to the genotype of the samples.

**Statistical analyses.** All statistical analyses were performed in Prism v.6.0 (GraphPad Software, Inc.) and SPSS v.21.0. No statistical methods were used to pre-determine sample sizes but our sample sizes are similar to those reported in previous publications[3,36,56,57]. The normality test was performed by the Shapiro–Wilk test. The homogeneity of variance test was performed by Levene's test. Data that met these two conditions were analyzed using a two-tailed unpaired or paired *t*-test, one-factor analysis of variance (ANOVA) and repeated-measures ANOVA followed by Tukey's multiple comparisons test. Data sets that were not normally distributed were analyzed with a nonparametric test (Supplementary Table 1). Values are expressed as the means ± s.e.m. All behavioral, electrophysiological, biochemical and morphological data were obtained by counterbalancing experimental conditions with controls. Details of particular statistical analyses can be found in Supplementary Tables 1 and 2. Statistical significance was accepted when $P < 0.05$.

**Reporting Summary.** Further information on research design is available in the Nature Research Reporting Summary linked to this article.

## Data availability

All supporting datasets generated or analyzed during the present study are available from the corresponding author upon reasonable request.

## References

50. Chen, Q. et al. Imaging neural activity using Thy1-GCaMP transgenic mice. *Neuron* **76**, 297–308 (2012).
51. Guo, B. et al. Chronic inflammatory pain impairs mGluR5-mediated depolarization-induced suppression of excitation in the anterior cingulate cortex. *Cereb. Cortex* **28**, 2118–2130 (2018).
52. Li, Y. et al. Serotonin neurons in the dorsal raphe nucleus encode reward signals. *Nat. Commun.* **7**, 10503 (2016).
53. Zhao, M. G. et al. Deficits in trace fear memory and long-term potentiation in a mouse model for fragile X syndrome. *J. Neurosci.* **25**, 7385–7392 (2005).
54. Jia, F. et al. Rapid and sparse labeling of neurons based on the mutant virus-like particle of Semliki forest virus. *Neurosci. Bull.* **35**, 378–388 (2019).
55. Ge, S. N. et al. Coexpression of VGLUT1 and VGLUT2 in trigeminothalamic projection neurons in the principal sensory trigeminal nucleus of the rat. *J. Comp. Neurol.* **518**, 3149–3168 (2010).
56. Matthews, G. A. et al. Dorsal raphe dopamine neurons represent the experience of social isolation. *Cell* **164**, 617–631 (2016).
57. Walsh, J. J. et al. 5-HT release in nucleus accumbens rescues social deficits in mouse autism model. *Nature* **560**, 589–594 (2018).

nature research

Corresponding author(s): Guoping Feng, Wenting Wang, Shengxi Wu

Last updated by author(s): May 27, 2019

# Reporting Summary

Nature Research wishes to improve the reproducibility of the work that we publish. This form provides structure for consistency and transparency in reporting. For further information on Nature Research policies, see Authors & Referees and the Editorial Policy Checklist.

## Statistics

For all statistical analyses, confirm that the following items are present in the figure legend, table legend, main text, or Methods section.

| n/a | Confirmed |
|---|---|
| ☐ | ☒ The exact sample size (*n*) for each experimental group/condition, given as a discrete number and unit of measurement |
| ☐ | ☒ A statement on whether measurements were taken from distinct samples or whether the same sample was measured repeatedly |
| ☐ | ☒ The statistical test(s) used AND whether they are one- or two-sided<br>*Only common tests should be described solely by name; describe more complex techniques in the Methods section.* |
| ☐ | ☒ A description of all covariates tested |
| ☐ | ☒ A description of any assumptions or corrections, such as tests of normality and adjustment for multiple comparisons |
| ☐ | ☒ A full description of the statistical parameters including central tendency (e.g. means) or other basic estimates (e.g. regression coefficient) AND variation (e.g. standard deviation) or associated estimates of uncertainty (e.g. confidence intervals) |
| ☐ | ☒ For null hypothesis testing, the test statistic (e.g. *F*, *t*, *r*) with confidence intervals, effect sizes, degrees of freedom and *P* value noted<br>*Give P values as exact values whenever suitable.* |
| ☒ | ☐ For Bayesian analysis, information on the choice of priors and Markov chain Monte Carlo settings |
| ☒ | ☐ For hierarchical and complex designs, identification of the appropriate level for tests and full reporting of outcomes |
| ☒ | ☐ Estimates of effect sizes (e.g. Cohen's *d*, Pearson's *r*), indicating how they were calculated |

*Our web collection on statistics for biologists contains articles on many of the points above.*

## Software and code

Policy information about availability of computer code

| | |
|---|---|
| Data collection | Clampex 10.6 was used for eletrophysiological data acquisition. Optical-tagging in vivo recording data was collected with OmniPlex 1.18 software.Confocal images were collected with FV10-ASW 04.02.01.20 software. Electron micrographs were captured with a Gatan digital 904 camera and its application software (832 SC1000). GCaMP3 signal of fiber photometry was converted to analogue voltage and digitalized with Spike2 8.08 software. |
| Data analysis | Imaris 7.7.1 software was used to reconstruct neuronal dendritic arbours, dendritic spines and sholl analysis. The western images and electron microscopy images were quantified using ImageJ 1.50d software. Clampfit 10.6 was used for eletrophysiological data off-line analysis. Matlab 2012 was used to analyse fiber photometry data. The behaviour data was analysed by Smart 3.0 software. All statistical analyses were performed in Prism 6.0 and SPSS 21.0. Optical-tagging in vivo recording data was analyzed with Offline sorter 4.0 and NeuroExplorer 5.0 software. |

For manuscripts utilizing custom algorithms or software that are central to the research but not yet described in published literature, software must be made available to editors/reviewers. We strongly encourage code deposition in a community repository (e.g. GitHub). See the Nature Research guidelines for submitting code & software for further information.

## Data

Policy information about availability of data

All manuscripts must include a data availability statement. This statement should provide the following information, where applicable:

- Accession codes, unique identifiers, or web links for publicly available datasets
- A list of figures that have associated raw data
- A description of any restrictions on data availability

The data that support the findings of this study are available from the corresponding author upon reasonable request.

# Field-specific reporting

Please select the one below that is the best fit for your research. If you are not sure, read the appropriate sections before making your selection.

☒ Life sciences ☐ Behavioural & social sciences ☐ Ecological, evolutionary & environmental sciences

For a reference copy of the document with all sections, see nature.com/documents/nr-reporting-summary-flat.pdf

# Life sciences study design

All studies must disclose on these points even when the disclosure is negative.

| | |
|---|---|
| Sample size | Sample size for each experiment is indicated in the figure legend for each experiment. The sample size was chosen based on previous experience for each experiment to yield high power to detect specific effects. No statistical methods were used to predetermine sample size. |
| Data exclusions | For in vitro eletrophysiological recordings, data were excluded when the resting membrane potential of neurons were positive than -60 mV and action potentials did not have overshoot or the series resistance changed by >20% to reject the unhealthy cell or bad recording based on previous study (PMID: 27018450, 28414301). Data were excluded only in experiments where viral injections were performed and post-hoc analysis of viral targeting demonstrated that injections were inaccurate. |
| Replication | All experiments were reliably reproduced in independent cells from independent mice (in vitro electrophysiology) or mice (behaviour,in vivo electrophysiology, fiber photometry, in situ hybridization histochemistry,immunofluorescence, western blot). Numbers of replicates (n) are indicated in the figure legends. |
| Randomization | Animals were chosen based on correct genotypes. Specifically, animal pairs from the same litters were compared to decrease variance in age and rearing. However, each experiment contained animals from at least two different litters to ensure that the differences between genotypes can be observed in mice from different litters. |
| Blinding | During the execution and analyses of the electrophysiological recordings, the electrophysiologist was blind to the genotypes of the individual animals. For in vivo immunohistochemistry and behaviour experiments, the investigator was blind to the experimental groups during the analyses. |

# Reporting for specific materials, systems and methods

We require information from authors about some types of materials, experimental systems and methods used in many studies. Here, indicate whether each material, system or method listed is relevant to your study. If you are not sure if a list item applies to your research, read the appropriate section before selecting a response.

## Materials & experimental systems

| n/a | Involved in the study |
|---|---|
| ☐ | ☒ Antibodies |
| ☐ | ☒ Eukaryotic cell lines |
| ☒ | ☐ Palaeontology |
| ☐ | ☒ Animals and other organisms |
| ☒ | ☐ Human research participants |
| ☒ | ☐ Clinical data |

## Methods

| n/a | Involved in the study |
|---|---|
| ☒ | ☐ ChIP-seq |
| ☒ | ☐ Flow cytometry |
| ☒ | ☐ MRI-based neuroimaging |

## Antibodies

| | |
|---|---|
| Antibodies used | The following primary antibodies were used for the morphology experiments:<br>rabbit anti-GFP antibody(Invitrogen, A11122, RRID:AB_221569, Lot: 1828014, 1:2000), peroxidase-conjugated antidigoxigenin antibody (Roche, 11207733910, Lot: 10520200, 1:2000), goat anti-GFP antibody (Rockland, 600101215, RRID:AB_218182, 1:800), rabbit anti-NeuN antibody (Millipore, ABN78, 1:500), mouse anti-GFAP antibody (Sigma, SAB1405864, 1:1000), goat anti-Iba1 antibody (Abcam, ab5076 , Lot: GR213536-1, 1:200), mouse anti-CaMKII antibody (Abcam, ab22609, Lot: GR300389, 1:200), mouse anti-GAD67 antibody (Millipore, MAB5406, Lot: 2581753, 1:1000), mouse anti-Shank3 (Neuromab, 75344, Lot: 455-2JD-24, 1:200).<br>The following primary antibodies were used for the western blot experiments: rabbit anti-Shank3 antibody (Santa Cruz, SC-30193, Lot: I0915, 1:200), rabbit anti-GluR1 antibody (Abcam, ab31232, Lot: GR321799-1, 1:200), rabbit anti-GluR2 antibody (Abcam, ab20673, 1:200), rabbit anti-NR1 antibody (Abcam, EPR2481, GR207980, 1:200), rabbit anti-NR2A antibody (Abcam, EPR2465, GR251596, 1:200), rabbit anti-NR2B antibody (Abcam, ab65783, Lot: GR3212648-1, 1:200), and mouse anti-β-actin antibody (Cell Signaling Technology, 3700, 1:500) |
| Validation | These references used the primary antibodies used in the current study:<br>rabbit anti-GFP antibody(Invitrogen, A11122, 1:2000) - J Comp Neurol 512(2): 141-157, (2009) PMID: 19003793, Cell 168(1-2): |

295-310 e219, (2017) PMID: 28041852.
peroxidase-conjugated antidigoxigenin antibody (Roche, 11207733910, Lot: 10520200, 1:2000) - Nat Commun 6: 8565, (2015) PMID: 26456232.
goat anti-GFP antibody (Rockland, 600101215, RRID:AB_218182, 1:800) - Nat Commun 6: 6349, (2015) PMID: 25695931.
rabbit anti-NeuN antibody (Millipore, ABN78, 1:500) - J Neuroinflammation 12: 86, (2015) PMID: 25953296.
mouse anti-GFAP antibody (Sigma, SAB1405864, 1:1000) - J Neurosci 34(2):346-355 (2014) PMID: 24403136.
goat anti-Iba1 antibody (Abcam, ab5076 , Lot: GR213536-1, 1:200) - J Neurosci 36(43): 11138-11150, (2016) PMID: 27798193.
mouse anti-CaMKII antibody (Abcam, ab22609, Lot: GR300389, 1:200) - Elife 5, (2016) PMID: 27328321, J Clin Invest 124(11): 5027-5036, (2014) PMID: 25295538.
mouse anti-GAD67 antibody (Millipore, MAB5406, Lot: 2581753, 1:1000) - Cell Res 24(6): 665-679, (2014) PMID: 24638034.
mouse anti-Shank3 (Neuromab, 75344, Lot: 455-2JD-24, 1:200) –J Neurosci 33(40): 15767-15778, (2013) PMID: 24089484.
rabbit anti-Shank3 antibody (Santa Cruz, SC-30193, Lot: I0915, 1:200) - Neuron 89(1):147-62, (2016) PMID:26687841.
rabbit anti-GluR1 antibody (Abcam, ab31232, Lot: GR321799-1, 1:200,) - Nat Neurosci 17(3): 367-376, (2014) PMID: 24464040.
rabbit anti-GluR2 antibody (Abcam, ab20673, 1:200) - J Neurosci 33(16): 6791-6799, (2013) PMID: 23595738.
rabbit anti-NR1 antibody (Abcam, EPR2481, GR207980, 1:200,) - Int J Dev Neurosci 54: 62-69, (2016) PMID: 27025552.
rabbit anti-NR2A antibody (Abcam, EPR2465, GR251596, 1:200) - Int J Dev Neurosci 54: 62-69, (2016) PMID: 27025552.
rabbit anti-NR2B antibody (Abcam, ab65783, Lot: GR3212648-1, 1:200) - Nat Neurosci 18(9): 1265-1271, (2015) PMID: 26280760.
mouse anti-β-actin antibody (Cell Signaling Technology, 3700, 1:500) - Nat Commun 7: 11385, (2016) PMID: 27150562.

## Eukaryotic cell lines

Policy information about cell lines

| | |
|---|---|
| Cell line source(s) | Mouse cell line NIH3T3 was obtained from ATCC (#CRL-1658) |
| Authentication | The cell line used has not been authenticated. |
| Mycoplasma contamination | The cell line tested negative for mycoplasma contamination. |
| Commonly misidentified lines (See ICLAC register) | No commonly misidentified cell lines were used in this study. |

## Animals and other organisms

Policy information about studies involving animals; ARRIVE guidelines recommended for reporting animal research

| | |
|---|---|
| Laboratory animals | Experimental mice included both males and females, between the ages of 2-6 months. The following strains were used: the Shank3B-/-, Shank3fx/fx and Thy1-GCaMP3 mouse strains were the gift from Guoping Feng Lab at MIT and all mice were bred onto a C57BL/6J background. |
| Wild animals | The study did not involve wild animals. |
| Field-collected samples | The study did not involve samples collected from the field. |
| Ethics oversight | All procedures were approved by the Institutional Animal Care and Use Committee (IACUC) at the Fourth Military Medical University (FMMU) and conformed to the Guide for the Care and Use of Laboratory Animals published by the National Institutes of Health (NIH). |

Note that full information on the approval of the study protocol must also be provided in the manuscript.